Journal of Computational Physics 229 (2010) 7774–7795

Contents lists available at ScienceDirect

Journal of Computational Physics

journal homepage: www.elsevier.com/locate/jcp

Multiple-relaxation-time lattice Boltzmann model for the convection and anisotropic diffusion equation

Hiroaki Yoshida *, Makoto Nagaoka

Toyota Central R&D Labs., Inc., Nagakute, Aichi 480-1192, Japan

ARTICLE INFO

Article history:
Received 25 January 2010
Received in revised form 22 June 2010
Accepted 23 June 2010
Available online 30 June 2010

Keywords:
Lattice Boltzmann method
Multiple-relaxation-time
Convection–diffusion equation
Anisotropy
Asymptotic analysis

ABSTRACT

A lattice Boltzmann model with a multiple-relaxation-time (MRT) collision operator for the convection–diffusion equation is presented. The model uses seven discrete velocities in three dimensions (D3Q7 model). The off-diagonal components of the relaxation-time matrix, which originate from the rotation of the principal axes, enable us to take into account full anisotropy of diffusion. An asymptotic analysis of the model equation with boundary rules for the Dirichlet and Neumann-type (specified flux) conditions is carried out to show that the model is first- and second-order accurate in time and space, respectively. The results of the analysis are verified by several numerical examples. It is also shown numerically that the error of the MRT model is less sensitive to the variation of the relaxation-time coefficients than that of the classical BGK model. In addition, an alternative treatment for the Neumann-type boundary condition that improves the accuracy on a curved boundary is presented along with a numerical example of a spherical boundary.
© 2010 Elsevier Inc. All rights reserved.

1. Introduction

The lattice Boltzmann method (LBM) [1,2] has emerged as an alternative numerical method for solving the Navier–Stokes type equations and has been extended to various types of flows, for example, turbulence [3,4], multi-phase systems [5–7], flows of multi-component fluids [8,9], micro scale flows [10–12] and flows through porous media [13–16]. Attempts have also been made to use the LBM to solve the convection–diffusion equation [17–25] and related equations, such as the pure diffusion equation [26,27] and the Poisson equation [28–30]. Although there are a vast number of alternative schemes for these equations associated with the finite element and finite-difference methods, the LBM is nevertheless attractive because it is easy to use for programming and is compatible with parallel computing. In addition, when we consider the diffusion phenomena in complex morphology, such as ion transport in the fuel cells [31,32] and secondary batteries [33], the LBM is a promising tool in view of the success in flows through porous media.

Most of the lattice Boltzmann models for the convection–diffusion equation are commonly limited to isotropic diffusion. This is because the Bathnagar–Gross–Krook (BGK) type model, which is the most commonly used collision model in the LBM, does not have sufficient parameters to describe anisotropic diffusion. Since anisotropy of diffusion plays a critical role in a variety of applications (see, e.g., Refs. [34,35]), removing this limitation is important. Recently, several groups have developed lattice Boltzmann models for anisotropic diffusion [36–40]. In particular, in Ref. [38] two types of models, referred to as equilibrium- and link-type models, with various sets of discrete velocities in two and three dimensions are described. These models can incorporate full anisotropy with off-diagonal components of the diffusion-coefficient tensor. However, the simplest models with five discrete velocities in two dimensions (D2Q5) and seven discrete velocities in three dimensions (D3Q7) are limited to the case of diagonal diffusion-coefficient tensors (DnQm denotes m discrete velocities in n dimensions).

* Corresponding author. Tel.: +81 561 71 7764; fax: +81 561 63 6920.
E-mail addresses: h-yoshida@mosk.tytlabs.co.jp (H. Yoshida), nagaoka@mosk.tytlabs.co.jp (M. Nagaoka).

0021-9991/$ - see front matter © 2010 Elsevier Inc. All rights reserved.
doi:10.1016/j.jcp.2010.06.037

In the present paper, we propose a lattice Boltzmann model for the convection–diffusion equation, which is based on the multiple-relaxation-time (MRT) method [9,12,41,42]. The number of tunable parameters in the MRT model is sufficient to cover the anisotropic diffusion-coefficient tensor. Using the MRT model provides an additional advantage over the BGK in that the error growth due to the variation of the relaxation coefficient is suppressed. Therefore, the model has an advantage even for isotropic diffusion, especially for the case in which the diffusion-coefficient varies temporally and/or spatially. Furthermore, since the present model requires only seven discrete velocities (D3Q7), the overhead in memory and CPU time is small compared to that of any other models using larger numbers of discrete velocities, such as the D3Q15 and D3Q19 models. The boundary rules for the D3Q7 model are also simple compared to those for other models [43–48], which further facilitates the implementation of the algorithm.

The classical Chapman–Enskog expansion technique is the most widely used method for analyzing the lattice Boltzmann equation (LBE) (see, e.g., Refs. [1,18,24,38]). Recently, a similar but essentially different technique referred to as asymptotic analysis has been proposed by Junk et al. [49,50]. Although the former is a powerful tool to show that the LBE reproduces certain partial differential equations, the dependence of the numerical solution on the expansion parameter is not immediately clear [51]. On the other hand, in the asymptotic analysis, the numerical solution itself is expanded in terms of powers of the small parameter representing the grid interval, and is analyzed order-by-order in the expansion. Therefore, clear information about the structure of the numerical solution is revealed. In the present study, we analyze the LBE and the boundary rules for the Dirichlet and the Neumann-type (specified flux) conditions by means of the asymptotic analysis. As a result, it is shown that the present model is first- and second-order accurate in time and space, respectively.

In engineering applications that involve complex geometries, the boundaries of the computational domain are curved [31–33]. In such cases, however, the straightforward application of the simple rule for the Neumann-type boundary condition mentioned above fails to capture the correct behavior of the macroscopic quantities, i.e., the numerical approximation does not converge to the exact solution no matter how high we make the grid resolution. The inherent difficulty stems from the fact that the surface area is overestimated when the boundary is approximated by the collection of the cube surfaces. We present an alternative treatment for curved Neumann-type boundaries, which circumvents this difficulty by introducing the local specific surface area. The signed distance function handled by the level set method (see, e.g., Ref. [52]) is used in the present paper to estimate the local specific surface area. We demonstrate the improvement by performing a numerical experiment for a simple problem with a reactive sphere.

The remainder of the present paper is organized as follows. In Section 2, after the convection–diffusion equation with the initial and boundary conditions is stated, the LBE with the classical BGK model and the proposed MRT model is described. We also present the computational procedure including the initialization and boundary rules. The analysis in Section 3 begins with re-scaling the time and spatial coordinates, followed by the asymptotic analysis of the LBE, the initialization rule, and the boundary rules, performed in that order. The results of the analysis are briefly summarized at the end of Section 3. In Section 4, we apply the proposed model to specific problems, namely, the Helmholtz equation, the Taylor–Aris dispersion problem, and the dispersion of a Gaussian hill. The treatment of curved Neumann-type boundaries is presented in Section 4.4 using the example of a spherical boundary. The Appendices describe a two-dimensional version of the present model (D2Q5) and outline the asymptotic analysis with a scaling different from that used in the main text.

2. Lattice Boltzmann method

2.1. The convection–diffusion equation

We consider the convection–diffusion equation (CDE) for $\phi(t,\mathbf{x})$ on a domain $\Omega \subset \mathbb{R}^3$ with the following initial condition:

$$\frac{\partial \phi}{\partial t} + \frac{\partial}{\partial x_j}(\phi v_j) = \frac{\partial}{\partial x_i}\left(D_{ij}\frac{\partial \phi}{\partial x_j}\right) + S, \tag{1}$$

$$\phi(0,\mathbf{x}) = \psi(\mathbf{x}), \tag{2}$$

where $t \in [0,\mathcal{T}]$ is the time, $\mathbf{x} \in \mathbb{R}^3$ is the spatial coordinate. (In the present paper, we either use boldface letters or assign indexes i, j, and k to designate the vector element in $\mathbb{R}^3$. We assume the summation convention for repeated indexes.) The diffusion-coefficient D_{ij} is a positive definite symmetric matrix. The initial value $\psi(\mathbf{x})$ and the source term $S(\phi)$ are given functions, and the background velocity $\mathbf{v}(t,\mathbf{x})$, which is assumed to be divergence-free, is also given.

On the boundary $\partial\Omega_d \subset \partial\Omega$, the Dirichlet boundary-value is given:

$$\phi = \Phi_d, \tag{3}$$

and on the boundary $\partial\Omega_n \subset \partial\Omega$, the Neumann-type boundary condition is imposed:

$$-n_i D_{ij}\frac{\partial \phi}{\partial x_j} + n_j v_j \phi = \Phi_n, \tag{4}$$

where $\mathbf{n}$ is the unit normal vector on $\partial\Omega_n$ pointing inward to the domain, and Φ_d and Φ_n are given functions of t and $\mathbf{x}$.

2.2. Lattice Boltzmann equation

The lattice Boltzmann equation (LBE) governs the behavior of the distribution function $f_\alpha(t,\mathbf{x})$, where $\alpha = 0,1,2,\ldots,6$. The sum of the distribution function $\phi = \sum_\alpha f_\alpha$ approximates the solution of the CDE. Each of f_α is transported over a regular spatial lattice with the assigned velocity. The direction of the velocity is defined in terms of the vector $\mathbf{e}_\alpha$. The set of $\mathbf{e}_\alpha$ is defined as (see Fig. 1)

$$[\mathbf{e}_0,\mathbf{e}_1,\mathbf{e}_2,\mathbf{e}_3,\mathbf{e}_4,\mathbf{e}_5,\mathbf{e}_6] = \begin{bmatrix} 0 & 1 & -1 & 0 & 0 & 0 & 0 \\ 0 & 0 & 0 & 1 & -1 & 0 & 0 \\ 0 & 0 & 0 & 0 & 0 & 1 & -1 \end{bmatrix}. \tag{5}$$

In the present paper, we use Greek subscripts to indicate the quantities corresponding to the directions of the discrete velocities, as f_α above. It is convenient to regard the quantities with the Greek index as vectors in $\mathbb{R}^7$. Thus, we introduce the following row and column vector notation:

$$\langle f| = (f_0,f_1,\ldots,f_6), \tag{6}$$

$$|f\rangle = (f_0,f_1,\ldots,f_6)^{\mathsf{T}}. \tag{7}$$

The LBE in the present model reads

$$|f\rangle(t+\Delta t,\mathbf{x}+\mathbf{e}_\alpha\Delta x) - |f\rangle(t,\mathbf{x}) = \mathsf{L}|f\rangle(t,\mathbf{x}) + \Delta t S|\omega\rangle, \tag{8}$$

where $|f\rangle(t+\Delta t,\mathbf{x}+\mathbf{e}_\alpha\Delta x)$ is the column vector having components $f_\alpha(t+\Delta t,\mathbf{x}+\mathbf{e}_\alpha\Delta x)$, and Δt and Δx are the time step and the grid interval, respectively. Here, $|\omega\rangle$ $(=(\omega_0,\omega_1,\ldots,\omega_6)^{\mathsf{T}})$ is the weight coefficient defined in Eqs. (13) through (15) below. The operator L is referred to as the collision operator, because this operator defines how f_α's interact during a time step. In the following subsection, we present an explicit expression of the collision operator of the Bathnagar–Gross–Krook (BGK) model, and we will later define the multiple-relaxation-time collision operator.

2.3. BGK model

The BGK model, which is the most widely used operator in the LBE, has the following form:

$$\mathsf{L}|f\rangle = \frac{1}{\tau}(|f^{\mathrm{eq}}\rangle - |f\rangle), \tag{9}$$

where τ is a coefficient that represents the relaxation-time relative to the time step. In this model, all the components of $|f\rangle$ relax to the equilibrium $|f^{\mathrm{eq}}\rangle$ with the single relaxation-time. In the present case of the convection–diffusion equation, $|f^{\mathrm{eq}}\rangle$ is defined as follows:

$$|f^{\mathrm{eq}}\rangle = \left(|\omega\rangle + \frac{\Delta t v_j}{\Delta x \mathcal{E}}|e_j\omega\rangle\right)\phi, \tag{10}$$

$$\phi = \langle 1|f\rangle, \tag{11}$$

where

$$\langle 1| = (1,1,1,1,1,1,1). \tag{12}$$

Here, $|\omega\rangle$ is a weight coefficient that satisfies the following conditions:

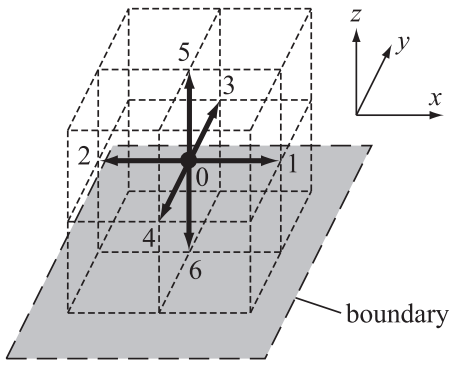

Fig. 1. Seven-velocity model in three dimensions (D3Q7 model). The gray-shaded plane indicates the boundary considered in Section 3.4.

$$\langle 1|\omega\rangle = 1, \tag{13}$$
$$\langle \mathbf{e}|\omega\rangle = 0, \tag{14}$$
$$\langle e_i e_j|\omega\rangle = \mathcal{E}\delta_{ij}, \tag{15}$$

where δ_{ij} is the Kronecker's delta, and the row vectors such as $\langle \mathbf{e}|$ are, according to the rule in Eq. (6),

$$\langle e_x| = (0,1,-1,0,0,0,0), \tag{16}$$
$$\langle e_y| = (0,0,0,1,-1,0,0). \tag{17}$$

In other words, they are the vectors for which the αth component is the quantity inside the brackets with the index α. If we choose, for instance, the weight coefficient to be

$$\omega_\alpha = \begin{cases} 1/4, & (\alpha = 0), \\ 1/8, & (\alpha = 1,\ldots,6), \end{cases} \tag{18}$$

then the coefficient of the tensor in Eq. (15) is $\mathcal{E} = 1/4$.

If we substitute Eqs. (10) and (11) into Eq. (9), then the BGK operator can be expressed in the following form:

$$\mathsf{L}|f\rangle = \frac{1}{\tau}\mathsf{Q}|f\rangle, \tag{19}$$
$$\mathsf{Q} = \left(|\omega\rangle + \frac{\Delta t v_j}{\Delta x \mathcal{E}}|e_j\omega\rangle\right)\langle 1| - \mathsf{I}, \tag{20}$$

where I is the 7×7 identity matrix.

2.4. Multiple-relaxation-time model

The basic process in the multiple-relaxation-time (MRT) model is as follows. (For MRT models for flow simulations, see, e.g., Refs. [12,41,42].) First, the vector $|f\rangle$ is projected onto the seven-dimensional vector space in which each component corresponds to a certain moment of $|f\rangle$. Then, we let each component relax to the equilibrium with a different relaxation coefficient. Finally, the vector is projected back onto the original seven-dimensional space. In contrast to the BGK model with the single relaxation coefficient, the MRT model allows us to tune the relaxation coefficient for each moment separately. This enables us to take anisotropy into account.

In the proposed MRT model, the collision operator in Eq. (8) is defined as follows:

$$\mathsf{L}|f\rangle = \mathsf{M}^{-1}\mathsf{S}\mathsf{M}\mathsf{Q}|f\rangle, \tag{21}$$

where the definition of the matrix Q is given by Eq. (20). Here, M is the matrix that projects a vector onto the moment space. We choose the following seven moments:

$$\begin{aligned}
&\langle 1|f\rangle\ (=\phi), && \langle 1| = (1,1,1,1,1,1,1),\\
&\langle e_x|f\rangle, && \langle e_x| = (0,1,-1,0,0,0,0),\\
&\langle e_y|f\rangle, && \langle e_y| = (0,0,0,1,-1,0,0),\\
&\langle e_z|f\rangle, && \langle e_z| = (0,0,0,0,0,1,-1),\\
&\langle 6-7\mathbf{e}^2|f\rangle, && \langle 6-7\mathbf{e}^2| = (6,-1,-1,-1,-1,-1,-1),\\
&\langle 3e_x^2-\mathbf{e}^2|f\rangle, && \langle 3e_x^2-\mathbf{e}^2| = (0,2,2,-1,-1,-1,-1),\\
&\left\langle e_y^2-e_z^2|f\right\rangle, && \langle e_y^2-e_z^2| = (0,0,0,1,1,-1,-1).
\end{aligned} \tag{22}$$

The first moment ϕ is the conserved quantity that approximates the solution to the CDE, whereas the second to fourth moments $\langle e_i|f\rangle$, which are first-order with respect to $\mathbf{e}$, are related to the flux of ϕ in the i direction. The vectors for the rest of the moments, $\langle 6-7\mathbf{e}^2|, \langle 3e_x^2-\mathbf{e}^2|$, and $\langle e_y^2-e_z^2|$, are obtained by means of Gram–Schmidt's method from $\langle \mathbf{e}^2|, \langle e_x^2|$, and $\langle e_y^2|$, respectively. A remark on the choice of these moments is given in Section 3.5. The matrix M is defined in terms of the moments in Eq. (22) as

$$\mathsf{M} = \begin{pmatrix} \langle 1| \\ \langle e_x| \\ \langle e_y| \\ \langle e_z| \\ \langle 6-7\mathbf{e}^2| \\ \langle 3e_x^2-\mathbf{e}^2| \\ \left\langle e_y^2-e_z^2\right| \end{pmatrix} = \begin{pmatrix} 1 & 1 & 1 & 1 & 1 & 1 & 1 \\ 0 & 1 & -1 & 0 & 0 & 0 & 0 \\ 0 & 0 & 0 & 1 & -1 & 0 & 0 \\ 0 & 0 & 0 & 0 & 0 & 1 & -1 \\ 6 & -1 & -1 & -1 & -1 & -1 & -1 \\ 0 & 2 & 2 & -1 & -1 & -1 & -1 \\ 0 & 0 & 0 & 1 & 1 & -1 & -1 \end{pmatrix}. \tag{23}$$

The definition of the relaxation-time matrix S is

$$\mathsf{S}^{-1} = \begin{pmatrix} \tau_0 & 0 & 0 & 0 & 0 & 0 & 0 \\ 0 & \bar{\tau}_{xx} & \bar{\tau}_{xy} & \bar{\tau}_{xz} & 0 & 0 & 0 \\ 0 & \bar{\tau}_{xy} & \bar{\tau}_{yy} & \bar{\tau}_{yz} & 0 & 0 & 0 \\ 0 & \bar{\tau}_{xz} & \bar{\tau}_{yz} & \bar{\tau}_{zz} & 0 & 0 & 0 \\ 0 & 0 & 0 & 0 & \tau_4 & 0 & 0 \\ 0 & 0 & 0 & 0 & 0 & \tau_5 & 0 \\ 0 & 0 & 0 & 0 & 0 & 0 & \tau_6 \end{pmatrix}. \tag{24}$$

The off-diagonal components correspond to the rotation of the principal axis of anisotropic diffusion. As shall be shown by applying the asymptotic analysis, if we set the values of the coefficients $\bar{\tau}_{ij}$ as in Eq. (25) below, the ϕ obtained using the proposed model approaches the solution to the CDE as $\Delta x \to 0$, keeping $\Delta t/\Delta x^2 =$ const.:

$$\bar{\tau}_{ij} = \frac{1}{2}\delta_{ij} + \frac{\Delta t}{\mathcal{E}\Delta x^2} D_{ij}. \tag{25}$$

The relaxation coefficient τ_0 for the conserved quantity ϕ does not affect the numerical solution. The remainder of the components of the relaxation-time matrix, τ_4, τ_5, and τ_6, have no effect on the leading-order approximation of the CDE solution, but affect the error terms.

2.5. Computational procedure

We now present the procedure for the implementation of the present LBM, including the initialization and the boundary rules.

(i) *Initial distribution*: the distribution of $|f\rangle(0,\mathbf{x})$ is given by the following equation using the initial condition $\psi(\mathbf{x}) = \phi(0,\mathbf{x})$.

$$|f\rangle(0,\mathbf{x}) = |\omega\rangle\psi + \left(\frac{\Delta t v_j}{\Delta x \mathcal{E}}\psi - \Delta x \frac{\partial \psi}{\partial x_j}\mathsf{M}^{-1}\mathsf{S}^{-1}\mathsf{M}\right)|e_j\omega\rangle. \tag{26}$$

(ii) *Collision*: the post-collision distribution, denoted by $|\hat{f}\rangle$, is given by

$$|\hat{f}\rangle(t,\mathbf{x}) = |f\rangle(t,\mathbf{x}) + \mathsf{L}|f\rangle(t,\mathbf{x}) + \Delta t S|\omega\rangle. \tag{27}$$

(iii) *Translation*: the value of $\hat{f}_\alpha$ is moved in the direction of $\mathbf{e}_\alpha$ by the distance Δx, i.e., we allow the post-collision values to travel to the neighboring nodes:

$$|f\rangle(t+\Delta t, \mathbf{x}+\mathbf{e}_\alpha\Delta x) = |\hat{f}\rangle(t,\mathbf{x}). \tag{28}$$

(iv) *Dirichlet boundary condition*: if the node from which the post-collision value travels ($\mathbf{x} - \mathbf{e}_\alpha \Delta x$) is outside the domain Ω through $\partial\Omega_d$, then the value of $f_\alpha(t+\Delta t,\mathbf{x})$ is given by the rule:

$$f_\alpha(t+\Delta t,\mathbf{x}) = -\hat{f}_\beta(t,\mathbf{x}) + \mathcal{E}\Phi_d. \tag{29}$$

Here, and in what follows, the index β indicates the direction opposite to α, i.e., $\mathbf{e}_\alpha = -\mathbf{e}_\beta$.

(v) *Neumann-type boundary condition*: if $\mathbf{x} - \mathbf{e}_\alpha\Delta x$ is outside the domain Ω through $\partial\Omega_n$, then the following rule applies:

$$f_\alpha(t+\Delta t,\mathbf{x}) = \hat{f}_\beta(t,\mathbf{x}) + \Delta t\Phi_n/\Delta x. \tag{30}$$

(vi) *Macroscopic quantity*: using the updated $|f\rangle$, the value of ϕ is computed from Eq. (11).

(vii) If $t + \Delta t$ reaches $\mathcal{T}$, or a specified convergence condition is satisfied in steady problems, then the computation is terminated; otherwise, processes (ii)–(vi) are repeated.

3. Asymptotic analysis

In this section, we carry out an asymptotic analysis of the lattice Boltzmann equation (LBE) and the initial- and boundary-condition treatments. Since the LBE of the present model is designed to capture diffusion phenomena, we should focus on the appropriate timescale in which diffusion is important. Keeping this in mind, we first perform the diffusive scaling of the time and spatial coordinates in the following subsection. We then analyze the re-scaled LBE applying the expansion technique proposed in Ref. [49]. An outline of the analysis of the initial and boundary rules is also presented, followed by a brief summary of the analytical results.

3.1. Diffusive scaling

Preliminary to the asymptotic analysis, we first re-scale the time and spatial coordinates, introducing the following dimensionless variables:

$$t' = \frac{U}{L}t, \quad \mathbf{x}' = \frac{1}{L}\mathbf{x}, \tag{31}$$

where L is the reference length and U is the reference speed. We can simply take a typical length characterizing the size of the domain Ω as the reference length L. In contrast, some considerations on the choice of the reference speed U are necessary. In the LBM, the distribution function f_α behaves like microscopic particles traveling over the lattice. Since each particle moves through the distance Δx during Δt, the speed characterizing the particle dynamics is $C = \Delta x/\Delta t$. We could simply take this speed C as the reference speed U for the scaling. In this case, the reference time, denoted by $T(=L/U)$, is the time interval taken for a particle to fly through the domain. However, the important timescale in the context of diffusion phenomena should be longer in view of the fact that the diffusion of a gas is much slower than the acoustic response, which is as fast as the motion of the gas molecules. Therefore, we allow U to be slower than C by applying the diffusive scaling [9,49,50] as described below. (A short note on the case in which $U = C$ is provided in Appendix B.) Diffusive scaling was first developed by Sone [53] to explain the connection between the Boltzmann equation and fluid-dynamic systems [54,55] and was later applied to the LBE to prove that the numerical solution converges to the incompressible Navier–Stokes equation [49,50,56].

In the asymptotic analysis, the following dimensionless parameter is introduced:

$$\epsilon = \frac{\Delta x}{L}. \tag{32}$$

This ϵ is used as the small parameter for the expansion. We will investigate the behavior of the LBE solution in the limit of $\epsilon \to 0$. This dimensionless parameter is very similar to the Knudsen number used in the kinetic theory of gases because Δx corresponds to the mean free path, which is the average distance between two successive collisions of a particle. It should be emphasized, however, that ϵ in the present analysis has no more physical meaning than the measure of the grid resolution. With this dimensionless parameter, we define the reference speed U as

$$U = C\epsilon. \tag{33}$$

This means we choose

$$T = \frac{L}{U} = \frac{\Delta t}{\epsilon^2}, \tag{34}$$

as the reference time, which is $1/\epsilon$ times longer than that in the case of $U = C$ (cf. Appendix B). Then, the dimensionless time defined in Eq. (31) becomes

$$t' = \frac{\epsilon^2}{\Delta t}t. \tag{35}$$

Correspondingly, the dimensionless time step, defined as $\delta t = \Delta t/T$, is equal to ϵ^2, i.e., $\delta t = \epsilon^2$ (see Eq. (34)). This means that, under the diffusive scaling, $\delta t/\epsilon^2$ must be maintained as unity in the limit of $\epsilon \to 0$.

Using these dimensionless variables, we re-scale the LBE (8) with the MRT collision operator (21), which leads to

$$|f\rangle(t' + \epsilon^2, \mathbf{x}' + \mathbf{e}_\alpha\epsilon) - |f\rangle(t', \mathbf{x}') = \mathsf{M}^{-1}\mathsf{S}\mathsf{M}\left(\mathsf{Q}^{(0)} + \epsilon\mathsf{Q}^{(1)}\right)|f\rangle(t', \mathbf{x}') + \epsilon^2\widetilde{S}|\omega\rangle, \tag{36}$$

where

$$\mathsf{Q}^{(0)} = |\omega\rangle\langle 1| - \mathsf{I}, \quad \mathsf{Q}^{(1)} = \tilde{v}_j|e_j\omega\rangle\langle 1|,$$
$$\tilde{v}_j = \frac{v_j}{U\mathcal{E}}, \quad \widetilde{S} = TS. \tag{37}$$

Note that $|f\rangle$ in Eq. (36) is regarded as a function of $(t', \mathbf{x}')$. In Sections 3.2 through 3.5, for the sake of notational simplicity, we drop the prime ($'$), and unless stated otherwise, the following replacements should be made:

$$t \to t', \quad \mathbf{x} \to \mathbf{x}'. \tag{38}$$

3.2. Asymptotic analysis of the LBE

We begin the analysis by expanding $|f\rangle$ in terms of powers of ϵ:

$$|f\rangle = |f^{(0)}\rangle + |f^{(1)}\rangle\epsilon + |f^{(2)}\rangle\epsilon^2 + \cdots \tag{39}$$

Correspondingly, ϕ is also expanded:

$$\phi = \phi^{(0)} + \phi^{(1)}\epsilon + \phi^{(2)}\epsilon^2 + \cdots \tag{40}$$

The relation between $|f^{(m)}\rangle$ and $\phi^{(m)}$ is obtained by substituting the expansions (39) and (40) into both sides of the definition $\phi = \langle 1|f\rangle$ (Eq. (11)) and equating the coefficients of the same power of ϵ:

$$\phi^{(m)} = \langle 1|f^{(m)}\rangle. \tag{41}$$

After inserting the expansion (39) into Eq. (36), the following Taylor expansion is applied:

$$|f^{(m)}\rangle(t+\epsilon^2, \mathbf{x}+\mathbf{e}_\alpha\epsilon) - |f^{(m)}\rangle(t,\mathbf{x}) = \frac{\partial|e_j f^{(m)}\rangle}{\partial x_j}\epsilon + \frac{\partial|f^{(m)}\rangle}{\partial t}\epsilon^2 + \frac{1}{2}\frac{\partial^2|e_i e_j f^{(m)}\rangle}{\partial x_i \partial x_j}\epsilon^2 + \frac{\partial^2|e_j f^{(m)}\rangle}{\partial t \partial x_j}\epsilon^3 + \frac{1}{2}\frac{\partial^2|f^{(m)}\rangle}{\partial t^2}\epsilon^4 + \frac{1}{6}\frac{\partial^3|e_i e_j e_k f^{(m)}\rangle}{\partial x_i \partial x_j \partial x_k}\epsilon^3 + \cdots \tag{42}$$

Equating the coefficients of the same power of ϵ leads to the following sequence of equations:

$$\text{order } \epsilon^0 : 0 = \mathsf{M}^{-1}\mathsf{S}\mathsf{M}\mathsf{Q}^{(0)}|f^{(0)}\rangle, \tag{43}$$

$$\text{order } \epsilon^1 : \frac{\partial|e_j f^{(0)}\rangle}{\partial x_j} = \mathsf{M}^{-1}\mathsf{S}\mathsf{M}\left(\mathsf{Q}^{(0)}|f^{(1)}\rangle + \mathsf{Q}^{(1)}|f^{(0)}\rangle\right), \tag{44}$$

$$\text{order } \epsilon^2 : \frac{\partial|f^{(0)}\rangle}{\partial t} + \frac{\partial|e_j f^{(1)}\rangle}{\partial x_j} + \frac{1}{2}\frac{\partial^2|e_i e_j f^{(0)}\rangle}{\partial x_i \partial x_j} = \mathsf{M}^{-1}\mathsf{S}\mathsf{M}\left(\mathsf{Q}^{(0)}|f^{(2)}\rangle + \mathsf{Q}^{(1)}|f^{(1)}\rangle\right) + \widetilde{S}|\omega\rangle, \tag{45}$$

$$\text{order } \epsilon^3 : \frac{\partial|f^{(1)}\rangle}{\partial t} + \frac{\partial|e_j f^{(2)}\rangle}{\partial x_j} + \frac{1}{2}\frac{\partial^2|e_i e_j f^{(1)}\rangle}{\partial x_i \partial x_j} + \frac{\partial^2|e_j f^{(0)}\rangle}{\partial t \partial x_j} + \frac{1}{6}\frac{\partial^3|e_i e_j e_k f^{(0)}\rangle}{\partial x_i \partial x_j \partial x_k} = \mathsf{M}^{-1}\mathsf{S}\mathsf{M}\left(\mathsf{Q}^{(0)}|f^{(3)}\rangle + \mathsf{Q}^{(1)}|f^{(2)}\rangle\right) + \widetilde{S}'\phi^{(1)}|\omega\rangle, \tag{46}$$

where $\widetilde{S}'$ is the derivative of $\widetilde{S}$ with respect to the argument corresponding to ϕ. The following two subsections are dedicated to solving Eqs. (43) and (44), whereas the CDE solved by the leading-order moment $\phi^{(0)}$ is derived from Eq. (45) in Section 3.2.3. In Section 3.2.4, using Eq. (46), the first-order moment $\phi^{(1)}$ is proven to vanish if the initial and boundary conditions are relevant.

3.2.1. Leading-order ϵ^0

Since the determinant of $\mathsf{Q}^{(0)}$ is zero, Eq. (43) has the non-trivial solution:

$$|f^{(0)}\rangle = |\omega\rangle\phi^{(0)}. \tag{47}$$

Here, we have used the following relation (see Eq. (37)):

$$\mathsf{Q}^{(0)}|f^{(m)}\rangle = (|\omega\rangle\langle 1| - \mathsf{I})|f^{(m)}\rangle = |\omega\rangle\phi^{(m)} - |f^{(m)}\rangle. \tag{48}$$

The moments of the leading-order solution, which will be used in the following subsections, are obtained explicitly as

$$\langle 1|f^{(0)}\rangle = \phi^{(0)}, \tag{49}$$

$$\langle e_i|f^{(0)}\rangle = 0, \tag{50}$$

$$\langle e_i e_j|f^{(0)}\rangle = \mathcal{E}\phi^{(0)}\delta_{ij}, \tag{51}$$

$$\langle e_i e_j e_k|f^{(0)}\rangle = 0. \tag{52}$$

3.2.2. First-order ϵ^1

Equation (44) is regarded as an equation for $|f^{(1)}\rangle$ because the leading-order solution $|f^{(0)}\rangle$ has been given. This is solved similarly to the leading-order equation:

$$|f^{(1)}\rangle = |\omega\rangle\phi^{(1)} + |e_j\omega\rangle\phi^{(0)}\tilde{\nu}_j - \mathsf{M}^{-1}\mathsf{S}^{-1}\mathsf{M}|e_j\omega\rangle\frac{\partial\phi^{(0)}}{\partial x_j}. \tag{53}$$

Here, we have used the following relation in addition to Eq. (48):

$$\mathsf{Q}^{(1)}|f^{(m)}\rangle = |e_j\omega\rangle\phi^{(m)}\tilde{\nu}_j. \tag{54}$$

The moments of the solution $|f^{(1)}\rangle$ are

$$\langle 1|f^{(1)}\rangle = \phi^{(1)}, \tag{55}$$

$$\langle e_i|f^{(1)}\rangle = \langle e_i|\omega\rangle\phi^{(1)} + \langle e_i|e_j\omega\rangle\phi^{(0)}\tilde{\nu}_j - \langle e_i|\mathsf{M}^{-1}\mathsf{S}^{-1}\mathsf{M}|e_k\omega\rangle\frac{\partial\phi^{(0)}}{\partial x_k} = \mathcal{E}\phi^{(0)}\tilde{\nu}_i - \bar{\tau}_{ij}\mathcal{E}\frac{\partial\phi^{(0)}}{\partial x_j}, \tag{56}$$

$$\langle e_i e_j|f^{(1)}\rangle = \mathcal{E}\phi^{(1)}\delta_{ij}. \tag{57}$$

In deriving these equations, the relations $\langle e_i|\mathsf{M}^{-1}\mathsf{S}^{-1}\mathsf{M}|e_k\omega\rangle = \bar{\tau}_{ij}\langle e_j|e_k\omega\rangle$ and $\langle e_i e_j|\mathsf{M}^{-1}\mathsf{S}^{-1}\mathsf{M}|e_k\omega\rangle = 0$, which are readily checked using the explicit form of the matrix M in Eq. (23), have been used.

3.2.3. Second-order ϵ^2—the convection–diffusion equation

We now note some properties of the collision operator. Since a simple calculation shows that $\langle 1|\mathsf{M}^{-1}\mathsf{SM} = (1/\tau_0)\langle 1|$, the following equations hold:

$$\langle 1|\mathsf{M}^{-1}\mathsf{SMQ}^{(0)} = 0, \tag{58}$$

$$\langle 1|\mathsf{M}^{-1}\mathsf{SMQ}^{(1)} = 0. \tag{59}$$

This set of the properties indicates that the conservation of ϕ during the collision process applies to any order of ϵ in the present analysis (unlike the Chapman–Enskog expansion); this is a consequence of the expansion of ϕ. Eq. (58) implies that the second-order Eq. (45) is only solvable under a certain constraint. To state this more specifically, we write Eq. (45) in a simple form: $\mathsf{M}^{-1}\mathsf{SMQ}^{(0)}|f^{(2)}\rangle = |b\rangle$, where $|b\rangle$ denotes the remaining terms. Taking the product of both sides with $\langle 1|$ leads to

$$\langle 1|\mathsf{M}^{-1}\mathsf{SMQ}^{(0)}|f^{(2)}\rangle = \langle 1|b\rangle = 0. \tag{60}$$

Here, $\langle 1|b\rangle$ contains the lower-order moments (49), (51) and (56). Inserting these moments into $\langle 1|b\rangle$ yields the explicit form of the constraint:

$$\frac{\partial \phi^{(0)}}{\partial t} + \frac{\partial}{\partial x_j}\left(\mathcal{E}\phi^{(0)}\tilde{v}_j\right) + \frac{\partial}{\partial x_i}\left[\left(-\bar{\tau}_{ij} + \frac{1}{2}\delta_{ij}\right)\mathcal{E}\frac{\partial \phi^{(0)}}{\partial x_j}\right] = \widetilde{S}. \tag{61}$$

If we relate the coefficients $\bar{\tau}_{ij}$ to the diffusion-coefficient tensor, as in Eq. (25), then Eq. (61) in the original dimensional coordinates (see Section 3.1) becomes

$$\frac{\partial \phi^{(0)}}{\partial t} + \frac{\partial}{\partial x_j}(\phi^{(0)} v_j) = \frac{\partial}{\partial x_i}\left(D_{ij}\frac{\partial \phi^{(0)}}{\partial x_j}\right) + S. \tag{62}$$

This means that the leading-order moment $\phi^{(0)}$ solves the CDE (1). In other words, the numerical solution $\phi = \phi^{(0)} + O(\epsilon)$ converges to the solution of the CDE in the limit of $\epsilon \to 0$ (keeping $\delta t/\epsilon^2 = 1$).

Under the restriction (61), the second-order Eq. (45) is solved for $|f^{(2)}\rangle$:

$$|f^{(2)}\rangle = |\omega\rangle\phi^{(2)} + |e_j\omega\rangle\phi^{(1)}\tilde{v}_j - \mathsf{M}^{-1}\mathsf{S}^{-1}\mathsf{M}\left(\frac{\partial|f^{(0)}\rangle}{\partial t} + \frac{\partial|e_j f^{(1)}\rangle}{\partial x_j} + \frac{1}{2}\frac{\partial^2|e_i e_j f^{(0)}\rangle}{\partial x_i \partial x_j} - \widetilde{S}|\omega\rangle\right). \tag{63}$$

Here, the relations (48) and (54) have been used. The moment of $|f^{(2)}\rangle$ to be used in the third-order analysis is obtained through a calculation similar to that in Eq. (56):

$$\langle e_i|f^{(2)}\rangle = \mathcal{E}\phi^{(1)}\tilde{v}_i - \bar{\tau}_{ij}\mathcal{E}\frac{\partial \phi^{(1)}}{\partial x_j}. \tag{64}$$

3.2.4. Third-order ϵ^3—accuracy of the LBE

Similarly to Eq. (45), the third-order Eq. (46) for $|f^{(3)}\rangle$ is only solvable under the constraint of the form $\langle 1|b\rangle = 0$, where $|b\rangle$ in turn denotes the terms in Eq. (46) other than $\mathsf{M}^{-1}\mathsf{SMQ}^{(0)}|f^{(3)}\rangle$. By using the expressions of the lower-order moments (50), (52), (55), (57) and (64), the specific form of the constraint is written as

$$\frac{\partial \phi^{(1)}}{\partial t} + \frac{\partial}{\partial x_j}\left(\mathcal{E}\phi^{(1)}\tilde{v}_j\right) + \frac{\partial}{\partial x_i}\left[\left(-\bar{\tau}_{ij} + \frac{1}{2}\delta_{ij}\right)\mathcal{E}\frac{\partial \phi^{(1)}}{\partial x_j}\right] = \widetilde{S}'\phi^{(1)}. \tag{65}$$

Since this equation for $\phi^{(1)}$ is linear and homogeneous, the solution is trivial, i.e., $\phi^{(1)} \equiv 0$, under the assumption that the boundary condition is also linear and homogeneous and the initial condition vanishes. We show in the following subsections that the assumption is true.

In the previous subsection, we have shown that $\phi^{(0)}$ solves the CDE. Thus, the remainder of the expansion (40) is interpreted as an error of the numerical scheme. The result $\phi^{(1)} = 0$ then means that the error is $O(\epsilon^2)$. In other words, with the relevant initial and boundary conditions, the present model possesses second-order accuracy with respect to ϵ or the grid interval. Note that, in view of $\delta t = \epsilon^2$ in the present scaling, the second-order accuracy with respect to ϵ also represents the first-order accuracy with respect to δt or the time step.

3.3. Analysis of the initial condition

In order to obtain the initial value of $\phi^{(m)}$, we substitute the expansion (39) into the left-hand side of the initialization rule (26). Equating the coefficients of the same power of ϵ gives

$$|f^{(0)}\rangle(0,\mathbf{x}) = |\omega\rangle\psi, \tag{66}$$

$$|f^{(1)}\rangle(0,\mathbf{x}) = \left(\psi\tilde{v}_j - \frac{\partial\psi}{\partial x_j}\mathsf{M}^{-1}\mathsf{S}^{-1}\mathsf{M}\right)|e_j\omega\rangle, \tag{67}$$

$$|f^{(m)}\rangle(0,\mathbf{x}) = 0 \ (m>1). \tag{68}$$

Note that the initial value of $|f^{(m)}\rangle$ is consistent with the asymptotic solution up to order ϵ (see Eqs. (47) and (53)). By inserting these relations into Eq. (41), we obtain

$$\phi^{(0)}(0,\mathbf{x}) = \psi(\mathbf{x}), \tag{69}$$

$$\phi^{(m)}(0,\mathbf{x}) = 0 \ (m>0). \tag{70}$$

3.4. Analysis of the boundary conditions

In this subsection, we analyze the boundary rules in Eqs. (29) and (30) in a manner similar to that described in Section 3.2 (see also Ref. [50]). Here, we restrict ourselves to the case of a plane boundary that is perpendicular to $\mathbf{e}_\alpha$ and passes through the midpoint between $\mathbf{x}$ and $\mathbf{x}-\mathbf{e}_\alpha\epsilon$. The case of curved boundaries will be considered in Section 4.4. In the following analysis, we assume $\alpha = 5$ (see Fig. 1). The analysis for the other values of α can be performed in a parallel manner.

The expansion is performed around the point on the boundary: $\mathbf{x}_B = \mathbf{x} - \mathbf{e}_5\epsilon/2 = \mathbf{x} + \mathbf{e}_6\epsilon/2$. Eqs. (29) and (30) are rewritten in terms of $\mathbf{x}_B$ as follows:

Dirichlet condition:

$$f_5\left(t+\epsilon^2, \mathbf{x}_B + \mathbf{e}_5\epsilon/2\right) = -f_6(t, \mathbf{x}_B - \mathbf{e}_6\epsilon/2) - \mathsf{L}|f\rangle_6(t, \mathbf{x}_B - \mathbf{e}_6\epsilon/2) - \epsilon^2\widetilde{S}\omega_6 + \mathcal{E}\Phi_d, \tag{71}$$

Neumann-type (specified flux) condition:

$$f_5\left(t+\epsilon^2, \mathbf{x}_B + \mathbf{e}_5\epsilon/2\right) = f_6(t, \mathbf{x}_B - \mathbf{e}_6\epsilon/2) + \mathsf{L}|f\rangle_6(t, \mathbf{x}_B - \mathbf{e}_6\epsilon/2) + \epsilon^2\widetilde{S}\omega_6 + \epsilon\widetilde{\Phi}_n, \tag{72}$$

where $\widetilde{\Phi}_n = \Phi_n/U$. The functions Φ_d and $\widetilde{\Phi}_n$ are evaluated at $\mathbf{x} = \mathbf{x}_B$. After inserting the expansions (39) into these equations, we further apply the following Taylor expansion:

$$f_5^{(m)}\left(t+\epsilon^2, \mathbf{x}_B + \mathbf{e}_5\epsilon/2\right) = f_5^{(m)} + \left(\frac{1}{2}\epsilon e_{5j}\frac{\partial}{\partial x_j} + \epsilon^2\frac{\partial}{\partial t} + \frac{1}{8}\epsilon^2 e_{5i}e_{5j}\frac{\partial^2}{\partial x_i\partial x_j} + \cdots\right)f_5^{(m)}, \tag{73}$$

$$f_6^{(m)}(t, \mathbf{x}_B - \mathbf{e}_6\epsilon/2) + \mathsf{L}|f^{(m)}\rangle_6(t, \mathbf{x} - \mathbf{e}_6\epsilon/2) = f_6^{(m)} + \mathsf{L}|f^{(m)}\rangle_6 + \left(-\frac{1}{2}\epsilon e_{6j}\frac{\partial}{\partial x_j} + \frac{1}{8}\epsilon^2 e_{6i}e_{6j}\frac{\partial^2}{\partial x_i\partial x_j} + \cdots\right)\left(f_6^{(m)} + \mathsf{L}|f^{(m)}\rangle_6\right). \tag{74}$$

(The set of arguments $(t, \mathbf{x}_B)$ is dropped for brevity.)

Equating the coefficients of the same power of ϵ gives sequences of the conditions that $\phi^{(m)}$ should satisfy. Let us examine these conditions for the Dirichlet and Neumann-type separately.

3.4.1. Dirichlet condition

The equation for the zeroth-order in ϵ is

$$f_5^{(0)} = -f_6^{(0)} - \mathsf{M}^{-1}\mathsf{S}\mathsf{M}\mathsf{Q}^{(0)}|f^{(0)}\rangle_6 + \mathcal{E}\Phi_d. \tag{75}$$

The second term in this equation vanishes because of the following relation:

$$\mathsf{Q}^{(0)}|f^{(0)}\rangle = 0. \tag{76}$$

This is easily derived from Eqs. (47) and (48). Then, by using the expression $f_5^{(0)} + f_6^{(0)} = \langle e_z^2|f^{(0)}\rangle = \mathcal{E}\phi^{(0)}$ (see Eq. (51)), Eq. (75) is transformed into

$$\phi^{(0)} = \Phi_d. \tag{77}$$

This shows that the leading-order solution $\phi^{(0)}$ satisfies the Dirichlet boundary condition.

Proceeding to order ϵ^1, we find

$$f_5^{(1)} + \frac{1}{2}e_{5j}\frac{\partial f_5^{(0)}}{\partial x_j} = -f_6^{(1)} - \mathsf{M}^{-1}\mathsf{S}\mathsf{M}\left(\mathsf{Q}^{(0)}|f^{(1)}\rangle_6 + \mathsf{Q}^{(1)}|f^{(0)}\rangle_6\right) + \frac{1}{2}e_{6j}\frac{\partial}{\partial x_j}\left(f_6^{(0)} + \mathsf{M}^{-1}\mathsf{S}\mathsf{M}\mathsf{Q}^{(0)}|f^{(0)}\rangle_6\right). \tag{78}$$

Substituting Eqs. (44) and (76) into the above expression yields

$$f_5^{(1)} + f_6^{(1)} + \frac{1}{2}\frac{\partial}{\partial x_j}\left(e_{5j} f_5^{(0)} + e_{6j} f_6^{(0)}\right) = 0. \tag{79}$$

Since the parenthesized terms cancel because of Eq. (47), the above equation is equivalent to

$$\phi^{(1)} = 0. \tag{80}$$

(Note that $f_5^{(1)} + f_6^{(1)} = \langle e_z^2 | f^{(1)} \rangle = \mathcal{E}\phi^{(1)}$. See Eq. (57)). This condition for $\phi^{(1)}$ guarantees that Eq. (65) has only a trivial solution.

3.4.2. Neumann-type (specified flux) condition

The zeroth-order terms in ϵ yield the following equation:

$$f_5^{(0)} = f_6^{(0)} + \mathsf{M}^{-1}\mathsf{S}\mathsf{M}\mathsf{Q}^{(0)} | f^{(0)} \rangle_6. \tag{81}$$

Since the second term vanishes (Eq. (76)) and $f_5^{(0)} = f_6^{(0)}$ (Eq. (47)), this condition is automatically satisfied, i.e., no condition for $\phi^{(m)}$ is obtained.

The terms of order ϵ^1 yield

$$f_5^{(1)} + \frac{1}{2} e_{5j} \frac{\partial f_5^{(0)}}{\partial x_j} = f_6^{(1)} + \mathsf{M}^{-1}\mathsf{S}\mathsf{M}\left(\mathsf{Q}^{(0)} | f^{(1)} \rangle_6 + \mathsf{Q}^{(1)} | f^{(0)} \rangle_6\right) - \frac{1}{2} e_{6j} \frac{\partial}{\partial x_j}\left(f_6^{(0)} + \mathsf{M}^{-1}\mathsf{S}\mathsf{M}\mathsf{Q}^{(0)} | f^{(0)} \rangle_6\right) + \widetilde{\Phi}_n. \tag{82}$$

By inserting Eqs. (44) and (76), we have

$$f_5^{(1)} - f_6^{(1)} + \frac{1}{2}\frac{\partial}{\partial x_j}\left(e_{5j} f_5^{(0)} - e_{6j} f_6^{(0)}\right) = \widetilde{\Phi}_n. \tag{83}$$

The first two terms are replaced by $\langle e_z | f^{(1)} \rangle$ (see Eq. (56)), and the sum in the parentheses is equal to $\langle e_z e_j | f^{(0)} \rangle$ (see Eq. (51)). Therefore, the condition is expressed as

$$\left(-\bar{\tau}_{zj} + \frac{1}{2}\delta_{zj}\right)\mathcal{E}\frac{\partial \phi^{(0)}}{\partial x_j} + \mathcal{E}\tilde{v}_z \phi^{(0)} = \widetilde{\Phi}_n. \tag{84}$$

Using the relation between $\bar{\tau}_{ij}$ and D_{ij} (Eq. (25)), we have

$$-D_{zj}\frac{\partial \phi^{(0)}}{\partial x_j} + v_z \phi^{(0)} = \Phi_n, \tag{85}$$

where $\mathbf{x}$ is the coordinate before re-scaling (see Eq. (31)). This indicates that $\phi^{(0)}$ satisfies the Neumann-type boundary condition.

Let us now proceed to order ϵ^2. Via similar calculations, which are omitted here for the sake of brevity, we obtain the following condition:

$$\left(-\bar{\tau}_{zj} + \frac{1}{2}\delta_{zj}\right)\frac{\partial \phi^{(1)}}{\partial x_j} + \tilde{v}_z \phi^{(1)} = 0. \tag{86}$$

Since the condition for $\phi^{(1)}$ is linear and homogeneous, the problem for $\phi^{(1)}$ has only a trivial solution (see Eqs. (65) and (70)).

3.5. Summary of the analysis

We now summarize the results of the asymptotic analysis.

(i) The leading-order coefficient $\phi^{(0)}$ is the solution to the following initial- and boundary-value problem:

$$\frac{\partial \phi^{(0)}}{\partial t} + \frac{\partial}{\partial x_j}\left(\mathcal{E}\phi^{(0)}\tilde{v}_j\right) + \frac{\partial}{\partial x_i}\left[\left(-\bar{\tau}_{ij} + \frac{1}{2}\delta_{ij}\right)\mathcal{E}\frac{\partial \phi^{(0)}}{\partial x_j}\right] = \widetilde{S}, \tag{87}$$

$$\phi^{(0)}(0, \mathbf{x}) = \psi(\mathbf{x}), \tag{88}$$

$$\phi^{(0)} = \Phi_d, \quad \mathbf{x} \in \partial\widetilde{\Omega}_d, \tag{89}$$

$$n_i\left(-\bar{\tau}_{ij} + \frac{1}{2}\delta_{ij}\right)\mathcal{E}\frac{\partial \phi^{(0)}}{\partial x_j} + \mathcal{E}n_j\tilde{v}_j\phi^{(0)} = \widetilde{\Phi}_n, \quad \mathbf{x} \in \partial\widetilde{\Omega}_n, \tag{90}$$

where $\partial\widetilde{\Omega}_d$ and $\partial\widetilde{\Omega}_n$ indicate the boundaries corresponding to $\partial\Omega_d$ and $\partial\Omega_n$, respectively, in the dimensionless space. Clearly, $\phi^{(0)}$ is the solution of the CDE problem (1)–(4) under the relation (25).

(ii) The coefficient of ϵ, or $\phi^{(1)}$, solves the following initial- and boundary-value problem:

$$\frac{\partial \phi^{(1)}}{\partial t} + \frac{\partial}{\partial x_j}\left(\mathcal{E}\phi^{(1)}\tilde{\nu}_j\right) + \frac{\partial}{\partial x_i}\left[\left(-\bar{\tau}_{ij} + \frac{1}{2}\delta_{ij}\right)\mathcal{E}\frac{\partial \phi^{(1)}}{\partial x_j}\right] = \widetilde{S}'\phi^{(1)}, \tag{91}$$

$$\phi^{(1)}(0,\mathbf{x}) = 0, \tag{92}$$

$$\phi^{(1)} = 0, \quad \mathbf{x} \in \partial\widetilde{\Omega}_d, \tag{93}$$

$$n_i\left(-\bar{\tau}_{ij} + \frac{1}{2}\delta_{ij}\right)\frac{\partial \phi^{(1)}}{\partial x_j} + n_j\tilde{\nu}_j\phi^{(1)} = 0, \quad \mathbf{x} \in \partial\widetilde{\Omega}_n. \tag{94}$$

Since the solution to this problem is trivial, or $\phi^{(1)} \equiv 0$, the expansion of ϕ becomes

$$\phi = \phi^{(0)} + \phi^{(2)}\epsilon^2 + \cdots \tag{95}$$

which means that the scheme is second-order accurate with respect to ϵ. Note that since $\delta t = \epsilon^2$ in the present scaling (see Section 3.1), it is first-order accurate with respect to δt.

The choice of the fifth to seventh moments in Eq. (22), which are second order with respect to **e**, does not affect the above results, as long as all of the moment vectors are orthogonal. In other words, we could choose another set of moment vectors, for instance, the orthogonal vectors constructed from $\langle e_x^2|$, $\langle e_y^2|$, and $\langle e_z^2|$ (instead of $\langle \mathbf{e}^2|$, $\langle e_x^2|$, and $\langle e_y^2|$, see Section 2.4). Even if we did so, the above results would be unaffected. However, the structure of the higher-order error terms, i.e., $\phi^{(m)}(m > 1)$, would change. Although it would be interesting to investigate the dependence of the error on the choice of the second-order moments, this is beyond the scope of the present paper.

Since the form of the discrete velocity vectors $|\mathbf{e}\rangle$ is not explicitly used in the asymptotic analysis in Section 3.2, models with another set of vectors could be analyzed in the same manner if they meet the constraints in Eqs.(49)–(52) and similar ones for higher-order moments. For example, the set of vectors of the D3Q15 model used in Ref. [42] is also applicable to the present model. Here, note that the constraints for the velocity vectors exclude the isotropy of the fourth-order tensor $\langle e_i e_j e_k e_l|\omega\rangle$, in contrast to the conventional LBM for the Navier–Stokes equation. This absence of constraint for the fourth-order tensor makes it possible to develop the model with the minimum number of discrete velocities, i.e., D3Q7 model.

Before closing this section, we discuss the approximation of the derivative $\partial\phi/\partial x_j$. The approximation of f_α up to order ϵ^2 is $|f\rangle = |f^{(0)}\rangle + |f^{(1)}\rangle\epsilon + |f^{(2)}\rangle\epsilon^2 + O(\epsilon^3)$. The explicit expressions of the coefficients $|f^{(0)}\rangle$, $|f^{(1)}\rangle$, and $|f^{(2)}\rangle$ have been obtained in Eqs. (47), (53) and (63), respectively. By taking the product with $\langle e_i|$ and solving for $\partial\,\phi^{(0)}/\partial x_j$, we find

$$\bar{\tau}_{ij}\frac{\partial \phi^{(0)}}{\partial x_j} = \tilde{\nu}_i\phi^{(0)} - \frac{1}{\mathcal{E}\epsilon}\langle e_i|f\rangle + O(\epsilon^2). \tag{96}$$

If we substitute the expansion (95) and neglect the term $O(\epsilon^2)$, we obtain the following formula:

$$\bar{\tau}_{ij}\frac{\partial \phi}{\partial x_j} = \frac{\Delta t\, v_i}{\mathcal{E}\Delta x^2}\phi - \frac{1}{\mathcal{E}\Delta x}\langle e_i|f\rangle, \tag{97}$$

where **x** is the coordinate before re-scaling (see Eq. (31)). Once we know f_α, the approximation of the derivative $\partial\phi/\partial x_j$ up to order ϵ is immediately obtained from Eq. (97).

4. Numerical examples

In this section, we apply the present model to a few specific problems. The main purpose of the test in Section 4.1 is to verify the applicability of the model to problems with various types of boundary conditions. The dependence of the error on the relaxation coefficient will also be investigated. The second and third examples involve background flows, i.e., convection as well as diffusion is taken into account. The anisotropic diffusion-coefficient tensors are considered in the third example. In the final example in Section 4.4, we consider the curved boundary on which the flux of ϕ is specified. The improved boundary rule for curved boundaries replacing Eq. (30) is also presented. All of the problems are described in terms of the time and spatial coordinates before re-scaling with arbitrary units.

4.1. Helmholtz equation

First, we consider the Helmholtz equation in the bounded domain:

$$\frac{\partial^2 \phi}{\partial x_j^2} = \kappa^2\phi, \quad x, y, z \in [0,1]. \tag{98}$$

The boundary conditions are

$$\frac{\partial\phi}{\partial x}(0,y,z) = -\mu\cos\pi y\sin\pi z, \quad \phi(1,y,z) = 0, \tag{99}$$

$$\phi(x,0,z) = \frac{\sinh\mu(1-x)\sin\pi z}{\cosh\mu}, \quad \phi(x,1,z) = -\frac{\sinh\mu(1-x)\sin\pi z}{\cosh\mu}, \tag{100}$$

$$\phi(x,y,0) = 0, \quad \phi(x,y,1) = 0, \tag{101}$$

where $\mu = \sqrt{\kappa^2 + 2\pi^2}$. This boundary-value problem has the following exact solution:

$$\phi_{\text{exact}} = \frac{\sinh\mu(1-x)\cos\pi y\sin\pi z}{\cosh\mu}. \tag{102}$$

We implement the LBM simulation with the initial condition $\phi = 0$ and regard the steady state as the numerical solution to the above problem. Since, in this case, the diffusion-coefficient tensor is $D_{ij} = \delta_{ij}$, the form of the corresponding relaxation coefficients is $\bar{\tau}_{ij} = \tau_D\delta_{ij}$ (see Eq. (25)). We place $N \times N \times N$ ($N = 5 \sim 80$) lattice points uniformly in the domain and use the value of Δt determined by Eq. (25). The computation is terminated when the difference between two successive values of ϕ reaches 10^{-8} at all of the lattice points.

In the multiple-relaxation-time (MRT) model, the relaxation coefficients that do not appear in the leading-order Eq. (61), τ_0, τ_4, τ_5, and τ_6, can be set independently of $\bar{\tau}_{ij} = \tau_D\delta_{ij}$. Throughout this section, the value of these coefficients is set to be unity unless stated otherwise:

$$\tau_p = 1, \quad (p = 0,4,5,6). \tag{103}$$

To measure the accuracy of the numerical solution, we use the following measure of error between the numerical solution $\phi_{\text{numerical}}$ and the exact solution:

$$E_2 = \left(\frac{1}{N^3}\sum_{x,y,z}(\phi_{\text{numerical}} - \phi_{\text{exact}})^2\right)^{1/2}. \tag{104}$$

Fig. 2 shows the log–log plot of E_2 versus the grid interval $\epsilon = 1/N$, for the case in which $\kappa = \pi$. For comparison, the results obtained using the classical BGK model ($\tau = \tau_D = \tau_p, p = 0,4,5,6$) are shown in Fig. 2(b). The line with a slope equal to 2 is also shown in each figure. Both models possess second-order accuracy with respect to the grid interval, as predicted in the previous section. In the case of the BGK model, some effects of the higher-order error occur in the range $\epsilon \geqslant 0.1$ for $\tau_D \geqslant 2.5$, whereas the second-order error is dominant in the entire range of ϵ for the MRT model. The error in both models increases as the value of τ_D increases, but the rate of increase is less for the MRT model. In order to examine the dependence of the error on τ_D in greater detail, we show E_2 versus τ_D for $\epsilon = 0.025$ in Fig. 3. The rate of error increase is clearly suppressed by using the MRT model.

As demonstrated by this example, the MRT collision model makes the numerical error less sensitive to the relaxation coefficient $\bar{\tau}_{ij} = \tau_D\delta_{ij}$. This is because keeping τ_p ($p = 4,5,6$) constant moderates the variation of the higher-order error ($\phi^{(2)}$). Therefore, even for an isotropic diffusion-coefficient the MRT model is still beneficial if τ_D is large. In the example of this subsection, increasing the value of τ_D corresponds to increasing the value of Δt because the relation (25) holds. Thus, Fig. 3 suggests that the computational time can be reduced using the MRT model with a larger value of Δt. For instance, if we

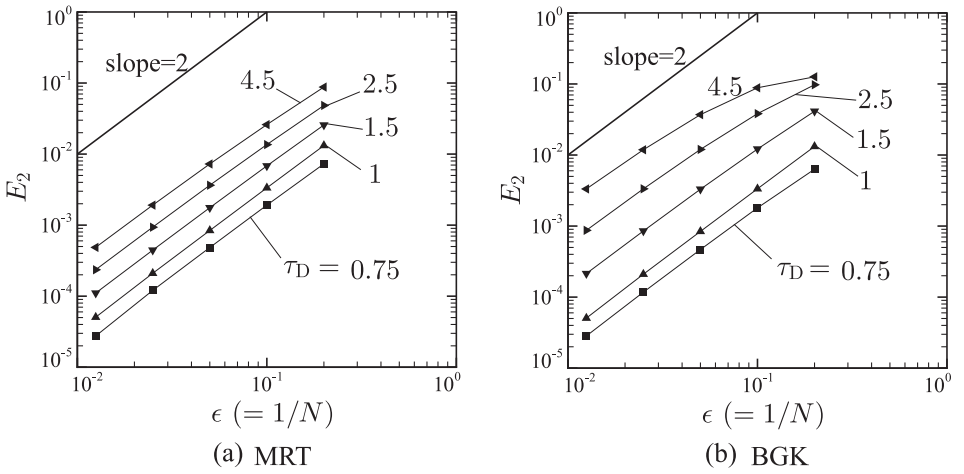

Fig. 2. E_2 versus $\epsilon = 1/N$ for various values of τ_D for the case of the Helmholtz equation. (a) Present multiple-relaxation-time (MRT) model. (b) BGK model. The line indicating a slope of 2 is also shown in the figure.

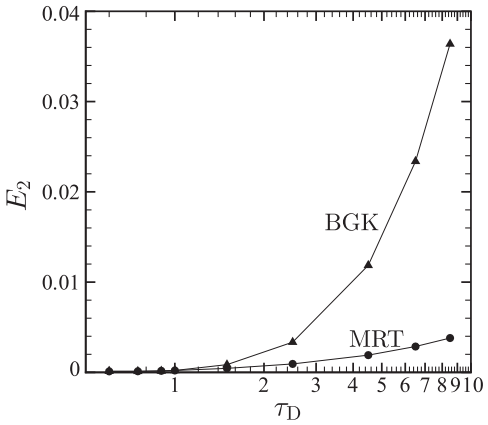

Fig. 3. E_2 versus τ_D for $\epsilon = 0.025$ for the case of the Helmholtz equation. The results of the present multiple-relaxation-time (MRT) model and the BGK model are shown.

allow the error to be comparable to that of the BGK model for $\tau_D = 2.5$ in Fig. 3, we can enlarge τ_D up to 8.5, which means that Δt can be four times as large as that for the BGK model (see Eq. (25)). The MRT model will also exhibit this advantage for the case in which the diffusion-coefficient varies temporally and/or spatially because τ_D can be large in such cases owing to the relation (25).

4.2. Taylor–Aris dispersion

As a second example, we consider the dispersion of the concentration ϕ under the background flow between two parallel plates, which is known as the Taylor–Aris dispersion problem [57,58]. More specifically, two plates perpendicular to the z direction are placed at $z = -1/2$ and $1/2$, and the solvent in the channel is flowing in the x direction. The flow velocity is $v_x(z) = 3\bar{v}(1 - 4z^2)/2,\ z \in [-1/2, 1/2]$, where $\bar{v}$ denotes the average velocity. The behavior of ϕ is governed by the convection–diffusion equation without the source term. The diffusion-coefficient tensor is assumed to be isotropic. In the long-time regime, the profile of ϕ averaged over the channel section, denoted by $\bar{\phi}(t,x)$, becomes approximately a Gaussian distribution irrespective of the initial condition. The longitudinal dispersion coefficient, defined as $D^{\mathrm{L}} = (1/2)\mathrm{d}(\sigma^2)/\mathrm{d}t$, measures the temporal growth of the variance σ^2. If we define the Péclet number as $\mathrm{Pe} = \bar{v}/D$, where D is the diffusion-coefficient, then the dispersion coefficient is analytically expressed as $D^{\mathrm{L}}{}_{\mathrm{analytical}} = D(1 + \mathrm{Pe}^2/210)$.

In the numerical simulation, we consider a channel of finite length, $x \in [0, L_x]$, and impose the periodic boundary condition at both ends. We assume the initial condition is uniform in y and symmetric with respect to the plane $z = 0$. The problem then reduces to a two-dimensional problem in x and z, and we need consider only the upper half of the channel, i.e., $z \in [0, 1/2]$. On the boundaries at $z = 0$ and $1/2$, the Neumann-type condition with no flux is imposed. The lattice points for the numerical computation are distributed in the x and z directions uniformly with the interval $\Delta x = 1/N$. Although there is only one layer of lattice points in the y direction, we use the present D3Q7 model with the periodic condition because the purpose of this example is to verify the model. The time step used in the following results is determined by Eq. (25) with $\tau_D = 0.6$. (Note that, in this problem, $D_{ij} = D\delta_{ij}$ and hence $\bar{\tau}_{ij} = \tau_{\mathrm{D}}\delta_{ij}$).

The dispersion process for the case of $\mathrm{Pe} = 50$ ($\bar{v} = 1$ and $D = 0.02$) and $N = 64$ is shown in Fig. 4. The contour shows the profiles of ϕ_{norm}, which is the concentration normalized by its maximum value. Starting from the one-dimensional initial condition, the profile of ϕ becomes two-dimensional because of the parabolic background flow. The distribution of the

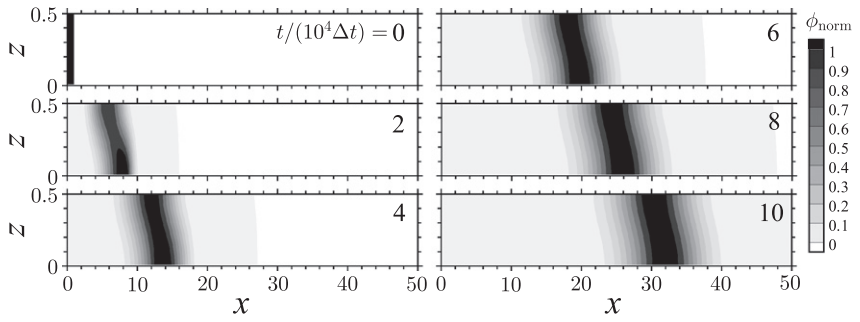

Fig. 4. Evolution of the concentration profile in the Taylor–Aris dispersion problem. $\mathrm{Pe} = 50$ ($\bar{v} = 1$ and $D = 0.02$) and $N = 64$. The profiles of ϕ_{norm} (ϕ normalized by its maximum value) at $t = 2n \times 10^4\Delta t$ ($n = 0 \sim 5$) are shown.

section-averaged concentration $\bar{\phi}$ is shown in Fig. 5. Here, $\bar{\phi}$ exhibits a Gaussian distribution after the initial deformation. The variance at any instant is numerically evaluated using the formula $\sigma^2 = g_{xx} - g_x^2$, where g_x and g_{xx} are the first- and second-order moments, respectively, of $\bar{\phi}(x)$, i.e., $g_x = (1/g_0)\int x\bar{\phi}\mathrm{d}x$ and $g_{xx} = (1/g_0)\int x^2\bar{\phi}\mathrm{d}x$ with $g_0 = \int \bar{\phi}\mathrm{d}x$. By taking the difference between the values of σ^2 at two different times t_1 and t_2, we obtain the numerical value of the dispersion coefficient, i.e., $D^{\mathrm{L}}_{\mathrm{numerical}} = \left[(\sigma^2)_{t=t_2} - (\sigma^2)_{t=t_1}\right]/2(t_2 - t_1)$. Table 1 lists the values of $D^{\mathrm{L}}_{\mathrm{numerical}}$ obtained in this manner with the analytic prediction $D^{\mathrm{L}}_{\mathrm{analytical}}$. Here, $L_x = 400$ for Pe = 160 and $L_x = 150$ otherwise. In computing σ^2 for Pe = 10, 50, and 160, we chose the values of t_1 and t_2 as $(t_1, t_2)/10^4\Delta t = (15,20)$, $(95,100)$, and $(190,200)$, respectively. Satisfactory agreement with the analytical prediction is observed in Table 1 up to Pe = 160.

In order to validate the second-order convergence predicted by the asymptotic analysis, we performed the simulations with various values of N. Fig. 6 shows the log–log plot of the relative error of $D^{\mathrm{L}}_{\mathrm{numerical}}/D$ from the analytical value versus the grid interval $\epsilon = 1/N$ for the case of Pe = 50. For comparison, the results obtained using the classical BGK model ($\tau = \tau_D = \tau_p, p = 0,4,5,6$) are shown in Fig. 6. (In Table 1, the relative error of the BGK model for $N = 64$ is shown in parentheses.) We further tested the other values of the relaxation coefficients, i.e., $\tau_D = 1.1$ with $\tau_p = 1.5$ ($p = 0,4,5,6$), and the results are shown in the same figure. In computing σ^2 for $\tau_D = 1.1$ with $N = 64$, we used $(t_1, t_2)/10^4\Delta t = (19,20)$. (Note that the time step for $\tau_D = 1.1$ is larger than $\tau_D = 0.6$.) In the case of $N = 32$ and 128, the same values of t_1 and t_2 as in the case of $N = 64$ were

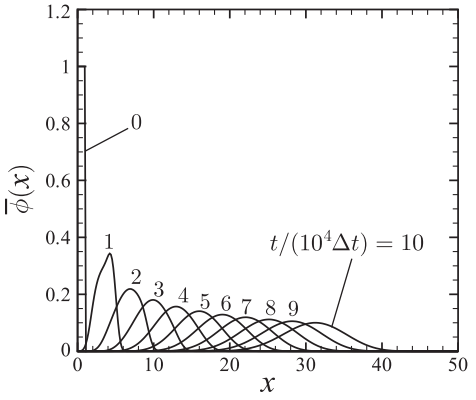

Fig. 5. Evolution of $\overline{\phi}(\phi$ averaged over the y–z section) in the Taylor–Aris dispersion problem. See the caption of Fig. 4 for the parameters.

Table 1
Taylor–Aris dispersion.

Pe	$D^{\mathrm{L}}_{\mathrm{numerical}}/D$	$D^{\mathrm{L}}{}_{\mathrm{analytical}}/D$	Error (%)
10	1.4752	1.4762	0.068
50	12.879	12.905	0.201 (0.240)*
160	121.78	122.90	0.911

*Error of the BGK model is in parentheses.

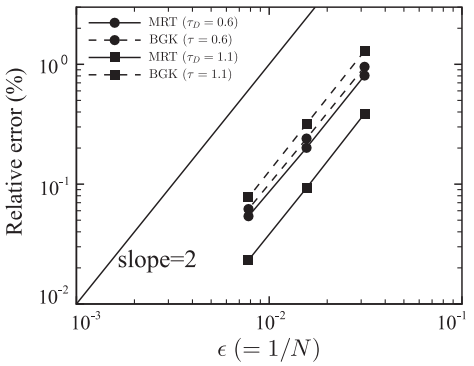

Fig. 6. Relative error of $D^{\mathrm{L}}_{\mathrm{numerical}}/D$ from the analytical value versus $\epsilon = 1/N$ in the Taylor–Aris dispersion problem. Pe = 50 ($\bar{v} = 1$ and $D = 0.02$). The results obtained using the present multiple-relaxation-time (MRT) model for the cases of $(\tau_D, \tau_p) = (0.6, 1)$ and $(1.1, 1.5)$ are indicated by ● and ■, respectively, with the solid line. The corresponding results obtained using the BGK model for $\tau = 0.6$ and 1.1 are indicated by ● and ■, respectively, with the dashed line.

used. In all cases, the error is proportional to $1/N^2$, and the magnitude of error is suppressed by using the MRT model. If we compare the results obtained by the MRT model for the two values of τ_D, we see that the magnitude of the error for $\tau_D = 1.1$ is smaller than that for $\tau_D = 0.6$. This is because of the different values of τ_p used ($\tau_p = 1$ in the latter case, see Section 4.1). Although the present paper concentrates on the validation of the second-order accuracy of the model, the optimization of the adjustable parameters τ_p, like the approach proposed by Lallemand and Luo [41], may further improve the accuracy of the MRT model.

4.3. Convection and anisotropic diffusion of a Gaussian hill

Next, we consider the time evolution of a Gaussian hill under a uniform flow. The x coordinate is taken along the flow, and the origin of the coordinates is at the center of the initial Gaussian, i.e., $\mathbf{v} = (v_x, 0, 0)$ and

$$\phi(0,\mathbf{x}) = \frac{\phi_0}{\left(2\pi\sigma_0^2\right)^{3/2}} \exp\left(-\frac{x_j^2}{2\sigma_0^2}\right), \tag{105}$$

where ϕ_0 is the total concentration, and σ_0^2 is the initial variance. The initial-value problem, Eq. (1) without the source term and Eq. (105), has the following exact solution:

$$\phi_{\text{exact}}(t,\mathbf{x}) = \frac{\phi_0}{(2\pi)^{3/2}\|\sigma_{ij}\|^{1/2}} \exp\left(-\frac{(\sigma^{-1})_{ij}(x_i - v_i t)(x_j - v_j t)}{2}\right), \tag{106}$$

where $\sigma_{ij} = \sigma_0^2\delta_{ij} - 2tD_{ij}$; $\|\sigma_{ij}\|$ is the absolute value of the determinant of σ_{ij}, and $(\sigma^{-1})_{ij}$ is the (i,j) component of the inverse of σ_{ij}.

In the LBM simulation, we consider the bounded domain, $x \in [-1/2, 3/2]$ and $y, z \in [-1, 1]$. The periodic boundary condition is imposed on the boundaries. Here, $2N \times 2N \times 2N$ lattice points are placed in the domain, and the time step is $\Delta t = 0.001 \times (10/N)^2$. In order to test the applicability to anisotropic diffusion, we consider the following three types of diffusion-coefficient tensors:

$$D_{ij} = \begin{pmatrix} 25^{-1/3} & 0 & 0 \\ 0 & 25^{-1/3} & 0 \\ 0 & 0 & 25^{-1/3} \end{pmatrix}, \quad \begin{pmatrix} \frac{1}{10} & 0 & 0 \\ 0 & \frac{2}{5} & 0 \\ 0 & 0 & 1 \end{pmatrix}, \quad \begin{pmatrix} \frac{1}{4} & -\frac{3\sqrt{2}}{40} & -\frac{3\sqrt{2}}{40} \\ -\frac{3\sqrt{2}}{40} & \frac{5}{8} & -\frac{3}{8} \\ -\frac{3\sqrt{2}}{40} & -\frac{3}{8} & \frac{5}{8} \end{pmatrix}. \tag{107}$$

The second type of diffusion-coefficient tensor possesses diagonal anisotropy, whereas the third type of diffusion-coefficient tensor has full anisotropy with off-diagonal components. The third tensor is the rotation of the second tensor by angle $\pi/6$ about z and x axes in this order. The relaxation coefficients are related to these diffusion-coefficient tensors via Eq. (25).

The numerical results for the case of $\phi_0 = 0.01$, $\sigma_0 = 0.02$, and $v_x = 10$ are shown in Fig. 7. In the figure, the profiles of ϕ at $t = 0.025$ in the x–z plane at $y = 0$ are shown, and the initial profile in the same plane is also shown in Fig. 7(a). Fig. 7(c) and (d) show that the present LBM successfully captures the convection and anisotropic diffusion process. Since the profile of ϕ is quite local in this problem, E_∞ defined below is more appropriate for investigating the accuracy than E_2 defined in Eq. (104):

$$E_\infty = \max_{x,y,z} |\phi_{\text{numerical}} - \phi_{\text{exact}}|. \tag{108}$$

We plot E_∞ as a function of $\epsilon = 1/N$ in Fig. 8. The values of the parameters used here are the same as those in Fig. 7. The figure confirms that the second-order accuracy of the present model is not violated by the anisotropy of the diffusion-coefficient tensor.

4.4. Surface reaction on a sphere

The final example involves a surface reaction on a sphere. Here, we consider the cubic domain $\Omega = \{\mathbf{x} | x \in [0,2];\ y, z \in [-1,1]\}$. On the boundaries at $x = 0$ and 2, the concentration is fixed at $\phi = 1$ and 0, respectively, and the Neumann-type condition with no flux is assumed on the rest of the boundaries. A sphere with radius R is located at the center of the domain. The surface reaction takes place on the sphere boundary $\partial\Omega_s = \{\mathbf{x} | (x-1)^2 + y^2 + z^2 = R^2\}$. The concentration flux is given by

$$-n_j D \frac{\partial \phi}{\partial x_j} = J_n, \quad \mathbf{x} \in \partial\Omega_s, \tag{109}$$

where $\mathbf{n}$ is the unit normal vector pointing inward to the domain, and D is the diffusion-coefficient, which is assumed to be isotropic in this example. Neither convection nor bulk reaction are considered here, i.e., $\mathbf{v} = 0$ and $S = 0$.

Let us denote by $\Delta\bar{J}$ the difference between the total fluxes flowing through the two fixed-concentration boundaries:

$$\Delta\bar{J} = J_{\text{out}} - J_{\text{in}}, \quad J_{\text{in}} = \int_{x=0} J_x \mathrm{d}y\,\mathrm{d}z, \quad J_{\text{out}} = \int_{x=2} J_x \mathrm{d}y\,\mathrm{d}z, \tag{110}$$

where $J_i = -D(\partial\phi/\partial x_i)$. The conservation law implies that in the steady state $\Delta\bar{J}$ is equal to the total flux from the sphere:

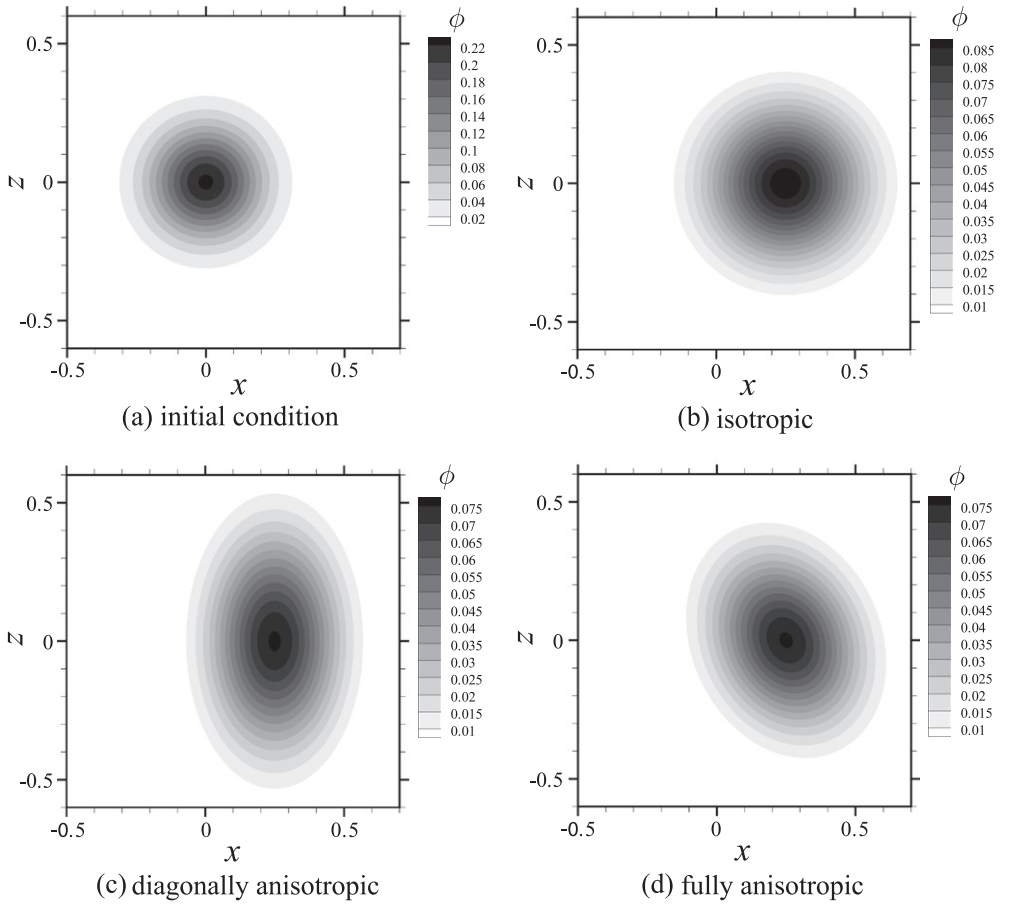

Fig. 7. Convection and diffusion of a Gaussian hill. $\phi_0 = 0.01, \sigma_0^2 = 0.02, v_x = 10$, and $N = 64$. The initial profile of ϕ in the x–z plane at $y = 0$ is shown in (a), and the corresponding profiles at $t = 0.025$ are shown in (b), (c), and (d). The diffusion-coefficient tensor is isotropic in (b), diagonally anisotropic in (c), and fully anisotropic in (d) (see Eq. (107)).

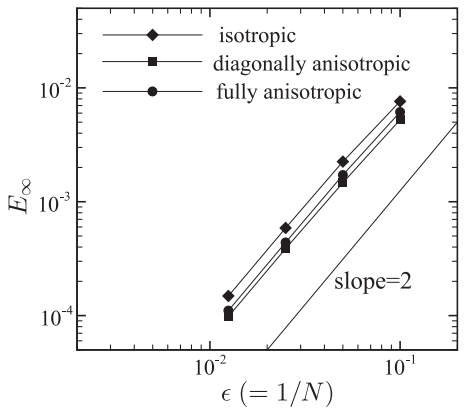

Fig. 8. E_∞ evaluated at $t = 0.025$ versus $\epsilon = 1/N$ for the case of convection and diffusion of a Gaussian hill. The results for the cases of isotropic (♦), diagonally anisotropic (■), and fully anisotropic (●) diffusion-coefficient tensors are shown. The line indicating a slope of 2 is also shown in the figure. See the caption of Fig. 7 for the other parameters.

$$\Delta\bar{J} = 4\pi R^2 J_n. \tag{111}$$

We use this relation for validation of the model. If we straightforwardly apply the procedure described in Section 2.5 to the present problem, the conservation law in Eq. (111) is not satisfied accurately, as shown in Fig. 9. The symbol □ indicates the results obtained using the rule in Eq. (30). The solid line indicates the analytical expression (111). The diffusion-coefficient

and the surface flux are fixed at $D = 1$ and $J_n = 0.5$. The disagreement arises from the fact that the surface area on which the reaction occurs is overestimated. More specifically, the surface of the sphere is approximated by the set of the cube surfaces with side length Δx when Eq. (30) is used. No matter how small we make Δx, the approximated area does not converge to the exact value. To avoid this difficulty, we use an alternative treatment for curved boundaries, as described below.

In the modified treatment, procedure (v) in Section 2.5 is replaced by.

- If $\mathbf{x} - \mathbf{e}_\alpha \Delta x$ is outside the cell boundary that envelopes the domain Ω (the thick line in Fig. 10(a)), then the rule in Eq. (30) with $\Phi_n = 0$ (bounce-back rule) is applied. (The *cell* of a lattice point refers to the cube box with side length Δx, the center of which is located at the lattice point.) Subsequently, on the lattice points of the cell that intersects the boundary (○ in Fig. 10(a)), Δf_α defined below is further added to $|f\rangle$:

$$\Delta f_\alpha = \begin{cases} \frac{A\Phi_n \Delta t}{\Delta x} \frac{(\mathbf{e}_\alpha \cdot \mathbf{n})}{\sum_\gamma \mathbf{e}_\gamma \cdot \mathbf{n}}, & (\text{if } \mathbf{e}_\alpha \cdot \mathbf{n} > 0), \\ 0, & (\text{otherwise}), \end{cases} \tag{112}$$

  where $A = A_c/\Delta x^2$, with A_c being the area of the intersection between the cell and the boundary. The summation is taken over γ such that $\mathbf{e}_\gamma \cdot \mathbf{n} > 0$.

In order to implement the above procedure, we need to prepare the normal $\mathbf{n}$ and the local specific surface area A assigned to each lattice point around the boundary. One method by which to do this is to use the signed distance function $\varphi(\mathbf{x})$ handled by the level set method [52]. The value of φ designates the distance from the boundary ($\varphi = 0$ for $\mathbf{x} \in \partial\Omega$), and the sign corresponds to the phase. Once we have φ, the normal $\mathbf{n}$ is obtained by taking the gradient. Here, A is estimated in the following manner. We consider the plane normal to $\mathbf{n}$ displaced by the distance $|\varphi|$ from the lattice point (see Fig. 10(b)). We approximate the area A_c by the area of the intersection between the plane and the cell, which can be easily calculated by splitting the polygon into triangles.

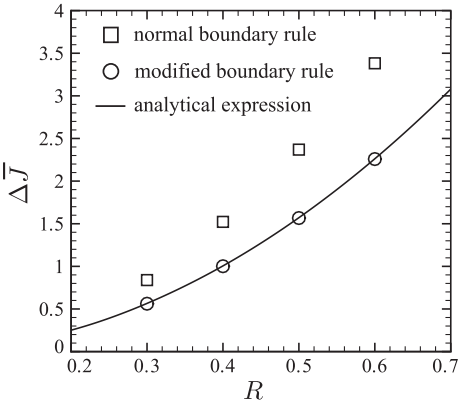

Fig. 9. Reaction flux from the sphere. $\Delta\bar{J}$ versus R for $D = 1$ and $J_n = 0.5$. The symbol □ indicates the results obtained using the normal boundary rule (30), and ○ indicates the results obtained using the modified boundary rule described in Section 4.4. The solid line indicates the analytical expression (110).

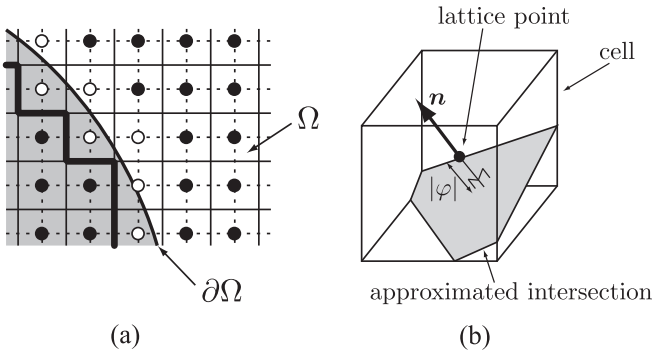

Fig. 10. (a) A two-dimensional schematic diagram of the lattice points around the curved boundary. The solid grid lines indicate the cell boundary, and the thick line indicates the cell boundary enveloping Ω. The black circle ● depicts the normal lattice points, and the white circle ○ depicts the lattice points of the cell that intersects the boundary $\partial\Omega$. (b) Approximated intersection in a cell.

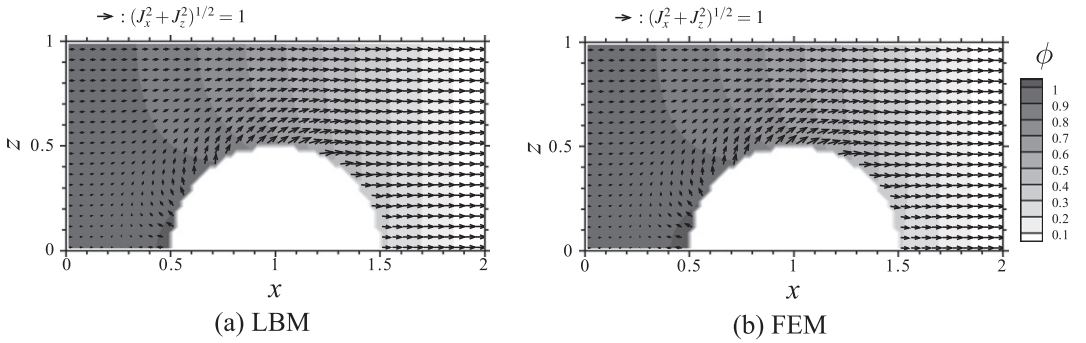

Fig. 11. Profiles of ϕ and vector fields of (J_x,J_z) in the x–z plane at $y = 0.0125$. $D = 1$, $J_n = 0.5$, and $R = 0.5$. (a) Present lattice Boltzmann method (LBM). (b) Finite element method (FEM).

When the boundary is expressed in an analytical form, φ is obtained immediately. In the present example, we have

$$\varphi(\mathbf{x}) = ((x-1)^2 + y^2 + z^2)^{1/2} - R, \quad \mathbf{n} = (n_x, n_y, n_z) = \frac{(x-1, y, z)}{((x-1)^2 + y^2 + z^2)^{1/2}}, \tag{113}$$

and the value of A is determined in the manner described above. On the other hand, if only a set of binary voxel data representing the shape of Ω is given, φ is obtained by applying an appropriate re-distancing procedure using the voxel data as the initial condition (see, e.g., Refs. [52,59]). For other methods of estimating $\mathbf{n}$ and A, see, e.g., Ref. [60].

In Fig. 9, the $\Delta\bar{J}$ obtained using the modified rule is also plotted with ○, and exhibits excellent agreement with the exact values. The profile of ϕ and the vector field of (J_x,J_z) in the x–z plane at $y = 0.0125$ in the case of $R = 0.5$ are shown in Fig. 11. For comparison, the corresponding figure obtained using the finite element method (FEM), is also shown. Although satisfactory agreement is achieved, there is a very slight discrepancy of the vectors near the sphere surface. This is because the flux tangential to the boundary surface is exposed to an unphysical restriction due to the bounce-back rule, unless the boundary is parallel to a symmetric axis of the lattice (cf. Ref. [47]). Further modification of the boundary rule to release this restriction, like the attempt made in Ref. [47], may improve the accuracy. Nevertheless, the overall agreement observed in Fig. 11 shows that the rule presented here is sufficient for practical applications.

In the numerical simulations for Figs. 9 and 11, we restricted the computational domain to one-quarter of the original domain, i.e., $x \in [0,2]$ and $y, z \in [0,1]$, considering the symmetry of the problem. The Neumann-type condition with no flux was imposed on the symmetry planes. In the LBM computations, $80 \times 40 \times 40$ lattice points were placed in the domain. The value of Δt was determined by Eq. (25) with $\bar{\tau}_{ij} = \delta_{ij}$. The computation was repeated until the difference between two successive values of ϕ was smaller than 10^{-8}. The FEM computation was performed using the 'COMSOL multiphysics' commercial solver. The subroutine called UMFPACK was used to solve the linear algebraic system. The number of elements was approximately 4.7×10^4, and the relative tolerance for the convergence judgment was 10^{-8}.

In concluding this section, we mention two of other methods to improve the accuracy on the Neumann-type boundary condition: one is the method proposed by Verhaeghe et al. [61], in which the value of f incoming from the boundary is estimated using a ghost node placed between the regular nodes; the value on the ghost node is interpolated from the neighboring regular nodes. Although the volume fraction field is utilized in expressing the curved boundary in Ref. [61], one can also implement the method using the signed distance function employed in the present paper. The other method, proposed by Izquierdo and Fueyo [62], is based on the finite-difference scheme for the macroscopic variable (ϕ in the present paper). The value on the boundary which is unknown in the case of Neumann condition is interpolated using the neighboring nodes; once the value of ϕ on the boundary is evaluated, the Dirichlet type treatment can be applied. Both methods also improve the accuracy on the Neumann-type boundary condition as described in Refs. [61,62]. One difference between these methods and the present one is that the latter possesses the localization of the scheme, i.e., the boundary treatment in the present method is implemented on each node without the aid of the neighboring nodes. The localization is necessary especially when the boundary is so complicated that the neighboring nodes can be outside the boundary. In addition, the localization allows us to easily parallelize the program code. In practical applications, one should choose an appropriate method for the problem under investigation, considering the pros and cons of the methods.

5. Concluding remarks

In the present paper, a lattice Boltzmann model for the convection and anisotropic diffusion equation has been proposed. The model is a straightforward extension of the BGK model to the multiple-relaxation-time model. By using the asymptotic analysis with the diffusive scaling, in Section 3, we demonstrated that the present model was second-order accurate in space. We carried out numerical simulations for specific problems in Section 4 and confirmed the analytical results. Since $\delta t = \epsilon^2$ in the diffusive scaling, the model is first-order accurate in time. In other words, we need to decrease δt while maintaining

$\delta t/\epsilon^2 = 1$ in order to increase the approximation accuracy. As noted in Appendix B, if we apply another scaling in which $\delta t = \epsilon$, the leading-order solution $\phi^{(0)}$ is proven to be a solution to the advection equation without the diffusion term. That is, if we let $\epsilon \to 0$ while maintaining $\delta t/\epsilon = 1$, then the numerical solution converges to the solution of the advection equation.

The classical Chapman–Enskog (CE) analysis is closely related to the asymptotic analysis [51]. Usually, the multiple-time-scale expansion technique using $T_2 = \Delta t/\epsilon^2$ and $T_1 = \Delta t/\epsilon$ is used in the CE analysis (see, e.g., Refs. [18,24,38]). The form of the derived partial differential equation depends on the choice of the reference time for scaling the terms related to $\mathbf{v}$ and S. If we choose T_2, then the equation corresponding to the set of Eqs. (87) and (91) is reproduced, whereas choosing T_1 leads to the equation corresponding to the set of Eqs. (B.5) and (B.6). In fact, if we merge the equations for $\phi^{(0)}$ and $\phi^{(1)}$ derived by means of the asymptotic analysis regarding $\phi^{(0)} + \epsilon\phi^{(1)}$ as ϕ, then we obtain exactly the same equations as those obtained with the CE analysis. However, in the CE analysis, the structure of the numerical solution is not immediately clear because all of the contributions of $f^{(m)}(m > 0)$ are included in ϕ, which is not expanded. On the other hand, as shown in Section 3.5, the asymptotic analysis provides the clear structure of the numerical solution, which is useful in the discussion of accuracy.

It was shown analytically in Section 3.4 and numerically in Section 4.1 that the boundary rules presented in Section 2.5 were second-order accurate with respect to the grid interval. However, the rule for the Neumann-type (specified flux) condition is not sufficiently accurate when the boundary is curved. An alternative treatment for curved Neumann-type boundaries, which improves the accuracy, was presented in Section 4.4. We demonstrated that the latter treatment provided acceptably accurate solutions. This treatment is particularly useful for applications that involve complex boundaries, such as a random porous structure, because even well established schemes such as the finite element method are not easily applied to such problems.

Finally, the structure of the errors, i.e., the specific forms of the equations for $\phi^{(m)}(m > 1)$, remains to be discussed. The higher-order errors are strongly affected by the adjustable relaxation coefficients τ_p $(p = 4,5,6)$, as deduced from Figs. 3 and 6. The optimal values of these adjustable parameters may be determined by applying, for example, the method proposed by Lallemand and Luo [41], in which the adjustable parameters in the MRT-LBM for the Navier–Stokes equation are optimized by investigating in detail the hydrodynamic behavior of the solution. An analysis of the higher-order equations for $\phi^{(m)}(m > 1)$ and investigation into the effect of the adjustable relaxation coefficients would pave the way for further improvement of accuracy of the method.

Acknowledgements

The authors are grateful to Dr. Hidemitsu Hayashi, Mr. Toshihisa Munekata, and Mr. Naoki Baba for the useful discussions.

Appendix A. Appendix A. D2Q5 model

We present a two-dimensional model with five discrete velocities (D2Q5) in the present multiple-relaxation-time formulation. Here, we summarize only the points that are different from the D3Q7 model. In the D2Q5 model, the directions of the discrete velocities are

$$[\mathbf{e}_0, \mathbf{e}_1, \mathbf{e}_2, \mathbf{e}_3, \mathbf{e}_4] = \begin{bmatrix} 0 & 1 & -1 & 0 & 0 \\ 0 & 0 & 0 & 1 & -1 \end{bmatrix}. \tag{A.1}$$

We give an example of the weight coefficient:

$$\omega_\alpha = \begin{cases} 1/3, & (\alpha = 0), \\ 1/6, & (\alpha = 1, \ldots, 4), \end{cases} \tag{A.2}$$

Then, the coefficient of the tensor in Eq. (15) is $\mathcal{E} = 1/3$.

The definition of the matrix M in Eq. (23) is replaced by

$$\mathsf{M} = \begin{pmatrix} \langle 1| \\ \langle e_x| \\ \langle e_y| \\ \langle 4 - 5\mathbf{e}^2| \\ \langle e_x^2 - e_y^2| \end{pmatrix} = \begin{pmatrix} 1 & 1 & 1 & 1 & 1 \\ 0 & 1 & -1 & 0 & 0 \\ 0 & 0 & 0 & 1 & -1 \\ 4 & -1 & -1 & -1 & -1 \\ 0 & 1 & 1 & -1 & -1 \end{pmatrix}. \tag{A.3}$$

The relaxation-time matrix S is defined as

$$\mathsf{S}^{-1} = \begin{pmatrix} \tau_0 & 0 & 0 & 0 & 0 \\ 0 & \bar{\tau}_{xx} & \bar{\tau}_{xy} & 0 & 0 \\ 0 & \bar{\tau}_{xy} & \bar{\tau}_{yy} & 0 & 0 \\ 0 & 0 & 0 & \tau_3 & 0 \\ 0 & 0 & 0 & 0 & \tau_4 \end{pmatrix}. \tag{A.4}$$

The relation between $\bar{\tau}_{ij}$ and D_{ij} is given by Eq. (25). By means of an analysis similar to that in Section 3, the model is shown to be first- and second-order accurate in time and space, respectively.

Appendix B. Scaling with $U = \Delta x/\Delta t$ and the advection equation

In Section 3.1, the speed $C\epsilon$ ($C = \Delta x/\Delta t$ and $\epsilon = \Delta x/L$) is taken as the reference speed. This leads to the relation $\delta t = \epsilon^2$, as discussed in Section 3.1. On the other hand, if we assume that the reference speed is C, we arrive at $\delta t = \epsilon$. Under the former relation, the convection–diffusion equation is derived from the lattice Boltzmann equation (LBE) as in Section 3.2. In this Appendix, we outline the asymptotic analysis under the latter relation. We show that the leading-order solution solves the advection equation instead of the convection–diffusion equation. The analysis proceeds in parallel with Section 3.2.

First, we rewrite the LBE in terms of the dimensionless variables defined in Eq. (31), noting that $U = C = \Delta x/\Delta t$. The re-scaled LBE then reads

$$|f\rangle(t'+\epsilon,\mathbf{x}'+\mathbf{e}_\alpha\epsilon) - |f\rangle(t',\mathbf{x}') = \mathsf{M}^{-1}\mathsf{S}\mathsf{M}\left(\mathsf{Q}^{(0)}+\mathsf{Q}^{(1)}\right)|f\rangle(t',\mathbf{x}') + \epsilon\widetilde{S}|\omega\rangle. \tag{B.1}$$

For the definitions of $\mathsf{Q}^{(0)}$, $\mathsf{Q}^{(1)}$, and $\widetilde{S}$, see Section 3.1.

We substitute the expansion (39) into Eq. (B.1) and subsequently apply the Taylor expansion to $|f^{(m)}\rangle(t'+\epsilon,\mathbf{x}'+\mathbf{e}_\alpha\epsilon)$. We then equate the coefficients of the same power of ϵ, to obtain the following sequence of equations. (In Eqs. (B.2) through (B.4) the prime ($'$) is dropped for simplicity.)

$$\text{order } \epsilon^0 : 0 = \mathsf{M}^{-1}\mathsf{S}\mathsf{M}\left(\mathsf{Q}^{(0)}+\mathsf{Q}^{(1)}\right)|f^{(0)}\rangle, \tag{B.2}$$

$$\text{order } \epsilon^1 : \frac{\partial|f^{(0)}\rangle}{\partial t} + \frac{\partial|e_j f^{(0)}\rangle}{\partial x_j} = \mathsf{M}^{-1}\mathsf{S}\mathsf{M}\left(\mathsf{Q}^{(0)}+\mathsf{Q}^{(1)}\right)|f^{(1)}\rangle + \widetilde{S}|\omega\rangle, \tag{B.3}$$

$$\text{order } \epsilon^2 : \frac{\partial|f^{(1)}\rangle}{\partial t} + \frac{\partial|e_j f^{(1)}\rangle}{\partial x_j} + \frac{1}{2}\frac{\partial^2|f^{(0)}\rangle}{\partial t^2} + \frac{\partial^2|e_j f^{(0)}\rangle}{\partial t\partial x_j} + \frac{1}{2}\frac{\partial^2|e_i e_j f^{(0)}\rangle}{\partial x_i\partial x_j} = \mathsf{M}^{-1}\mathsf{S}\mathsf{M}\left(\mathsf{Q}^{(0)}+\mathsf{Q}^{(1)}\right)|f^{(2)}\rangle + \widetilde{S}'\phi^{(1)}|\omega\rangle. \tag{B.4}$$

In the same manner as described in Section 3.2, these equations are solved successively from the lowest order. As explained in Section 3.2.3, certain restrictions that form the partial differential equations for $\phi^{(0)}$ and $\phi^{(1)}$ must be satisfied so that Eqs. (B.3) and (B.4) have solutions. Their explicit expressions are

$$\frac{\partial\phi^{(0)}}{\partial t} + \frac{\partial}{\partial x_j}\left(\mathcal{E}\phi^{(0)}\tilde{v}_j\right) = \widetilde{S}, \tag{B.5}$$

$$\frac{\partial\phi^{(1)}}{\partial t} + \frac{\partial}{\partial x_j}\left(\mathcal{E}\phi^{(1)}\tilde{v}_j\right) + \frac{\partial}{\partial x_i}\left[\left(-\bar{\tau}_{ij}+\frac{1}{2}\delta_{ij}\right)\mathcal{E}\frac{\partial\phi^{(0)}}{\partial x_j}\right] + \frac{\partial}{\partial x_i}\left[\left(-\bar{\tau}_{ij}+\frac{1}{2}\delta_{ij}\right)\mathcal{E}\frac{\partial\phi^{(0)}\tilde{v}_j}{\partial t}\right] + \frac{1}{2}\frac{\partial\widetilde{S}}{\partial t} = \widetilde{S}'\phi^{(1)}. \tag{B.6}$$

Eq. (B.5) is an advection equation with the source term. Therefore, the numerical solution ϕ converges to the solution of the advection equation as $\epsilon \to 0$. Note that, since the relation $\delta t = \epsilon$ holds in the scaling, the limit must be taken while maintaining $\delta t/\epsilon = 1$ or $\Delta t/\Delta x = \text{const}$. Eq. (B.6) for $\phi^{(1)}$ has a non-trivial solution because it contains inhomogeneous terms. Thus, the approximation to the solution of the advection equation is only first-order accurate both in time and space.

In order to verify the results of the analysis, we consider a problem similar to that described in Section 4.3. Here, we use t and $\mathbf{x}$ before re-scaling. The behavior of ϕ is described by the pure advection equation:

$$\frac{\partial\phi}{\partial t} + \frac{\partial}{\partial x_j}(\phi v_j) = 0. \tag{B.7}$$

The initial condition is given by Eq. (105). Then, the exact solution is

$$\phi_{\text{exact}}(t,\mathbf{x}) = \frac{\phi_0}{\left(2\pi\sigma_0^2\right)^{3/2}}\exp\left(-\frac{(x_j - v_j t)^2}{2\sigma_0^2}\right). \tag{B.8}$$

The LBM simulation is carried out restricting the computational domain to $\Omega = \{\mathbf{x} | x \in [-1/2, 3/2];\ y, z \in [-1/2, 1/2]\}$ in which $2N \times N \times N$ lattice points are distributed uniformly. The time step is kept at $\Delta t = 0.01/N$, and the relaxation coefficients are fixed at $\bar{\tau}_{ij} = \tau_D\delta_{ij}$ with $\tau_D = 0.6$ or 1.1. The computational procedure is the same as that described in Section 2.5, except that Eq. (26) is replaced by

$$|f\rangle(0,\mathbf{x}) = |\omega\rangle\psi + \frac{\Delta t v_j}{\Delta x\mathcal{E}}\psi|e_j\omega\rangle. \tag{B.9}$$

The values of the other parameters are the same as those in Section 4.3. The solution at $t = 0.025$ is compared to the exact solution (B.8). Fig. 12 shows the log–log plot of E_∞ (see Eq. (108)) versus the grid interval $\epsilon = 1/N$. The line with a slope equal to unity is also shown. As the value of $1/N$ decreases, the numerical solution tends to approach the solution of the advection equation with the leading error proportional to $1/N$. The deviation from the first-order convergence for the large values of $1/N$ implies that the error due to the higher-order terms is rather significant.

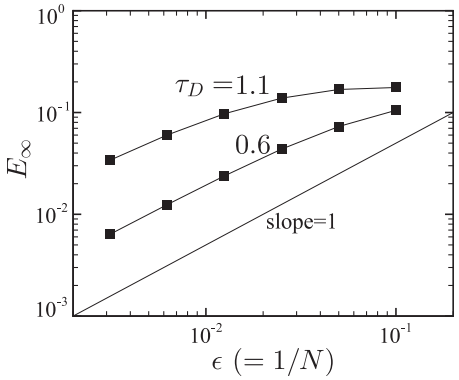

Fig. 12. E_∞ (Eq. (108)) evaluated at $t = 0.025$ versus $\epsilon = 1/N$ in the case of pure advection of a Gaussian hill. $\phi_0 = 0.01, \sigma_0^2 = 0.02$, and $v_x = 10$. The line indicating a slope of unity is also shown in the figure.

In the limit $\Delta x \to 0$ keeping $\Delta t/\Delta x =$ const, the diffusion-coefficient tensor D_{ij} should vanish under relation (25) (provided that the values of $\bar{\tau}_{ij}$ are finite). This also implies that the numerical solution converges to the solution of the advection equation in such a limit. If we attempt to solve the convection–diffusion equation with $\Delta t \propto \Delta x$, we need to tune the values of $\bar{\tau}_{ij}$ so that D_{ij} is maintained constant. Fig. 3 suggests that even if the values of $\bar{\tau}_{ij}$ become large owing to such a tuning, the increase in the error (of order ϵ^2) is suppressed by using the multiple-time-relaxation model.

References

[1] S. Chen, G.D. Doolen, Lattice Boltzmann method for fluid flows, Annu. Rev. Fluid Mech. 30 (1998) 329–364.
[2] S. Succi, The Lattice Boltzmann Equation for Fluid Dynamics and Beyond, Oxford University Press, New York, 2001.
[3] J. Lätt, B. Chopard, S. Succi, F. Toschi, Numerical analysis of the averaged flow field in a turbulent lattice Boltzmann simulation, Physica A 362 (2006) 6–10.
[4] H. Yu, L.-S. Luo, S.S. Girimaji, LES of turbulent square jet flow using an MRT lattice Boltzmann model, Comput. Fluids 35 (2006) 957–965.
[5] T. Inamuro, T. Ogata, S. Tajima, N. Konishi, A lattice Boltzmann method for incompressible two-phase flow with large density differences, J. Comput. Phys. 198 (2004) 628–644.
[6] H.W. Zheng, C. Shu, Y.T. Chew, A lattice Boltzmann model for multiphase flows with large density ratio, J. Comput. Phys. 218 (2006) 353–371.
[7] K.N. Premnath, J. Abraham, Three-dimensional multi-relaxation time (MRT) lattice-Boltzmann models for multiphase flow, J. Comput. Phys. 224 (2007) 539–559.
[8] L.-S. Luo, S.S. Girimaji, Theory of the lattice Boltzmann method: two-fluid model for binary mixtures, Phys. Rev. E 67 (2003) 036302.
[9] P. Asinari, Asymptotic analysis of multiple-relaxation-time lattice Boltzmann schemes for mixture modeling, Comput. Math. Appl. 55 (2008) 1392–1407.
[10] Z. Guo, T.S. Zhao, Y. Shi, Physical symmetry, spatial accuracy, and relaxation time of the lattice Boltzmann equation for microgas flows, J. Appl. Phys. 99 (2006) 074903.
[11] X.-D. Niu, S. Hyodo, T. Munekata, K. Suga, Kinetic lattice Boltzmann method for microscale gas flows: issues on boundary condition, relaxation time, and regularization, Phys. Rev. E 76 (2007) 036711.
[12] Z. Guo, C. Zheng, B.C. Shi, Lattice Boltzmann equation with multiple effective relaxation times for gaseous microscale flow, Phys. Rev. E 77 (2008) 036707.
[13] Z. Guo, T.S. Zhao, Lattice Boltzmann model for incompressible flows through porous media, Phys. Rev. E 66 (2002) 036304.
[14] C. Pan, L.-S. Luo, C.T. Miller, An evaluation of lattice Boltzmann schemes for porous medium flow simulation, Comput. Fluids 35 (2006) 898–909.
[15] J. Psihogios, M.E. Kainourgiakis, A.G. Yiotis, A.T. Papaioannou, A.K. Stubos, A lattice Boltzmann study of non-Newtonian flow in digitally reconstructed porous domains, Transp. Porous Med. 70 (2007) 279–292.
[16] Q. Kang, P.C. Lichtner, D. Zhang, An improved lattice Boltzmann model for multicomponent reactive transport in porous media at the pore scale, Water Resour. Res. 43 (2007) W12S14.
[17] E.G. Flekkøy, Lattice Bhatnagar–Gross–Krook models for miscible fluids, Phys. Rev. E 47 (1993) 4247–4257.
[18] S.P. Dawson, S. Chen, G.D. Doolen, Lattice Boltzmann computations for reaction–diffusion equations, J. Chem. Phys. 98 (1993) 1514–1523.
[19] H.W. Stockman, R.J. Glass, C. Cooper, H. Rajaram, Accuracy and computational efficiency in 3D dispersion via lattice-Boltzmann: models for dispersion in rough fractures and double-diffusive fingering, Int. J. Mod. Phys. C 9 (1998) 1545–1557.
[20] R. Blaak, P.M.A. Sloot, Lattice dependence of reaction-diffusion in lattice Boltzmann modeling, Comput. Phys. Commun. 129 (2000) 256–266.
[21] R.G.M. van der Sman, M.H. Ernst, Convection–diffusion lattice Boltzmann scheme for irregular lattices, J. Comput. Phys. 160 (2000) 766–782.
[22] R.M.H. Merks, A.G. Hoekstra, P.M.A. Sloot, The moment propagation method for advection–diffusion in the lattice Boltzmann method: validation and Péclet number limits, J. Comput. Phys. 183 (2002) 563–576.
[23] M. Stiebler, J. Tölke, M. Krafczyk, Advection–diffusion lattice Boltzmann scheme for hierarchical grids, Comput. Math. Appl. 55 (2008) 1576–1584.
[24] B.C. Shi, B. Deng, R. Du, X.W. Chen, A new scheme for source term in LBGK model for convection–diffusion equation, Comput. Math. Appl. 55 (2008) 1568–1575.
[25] B.C. Shi, Z. Guo, Lattice Boltzmann model for nonlinear convection–diffusion equations, Phys. Rev. E 79 (2009) 016701.
[26] D. Wolf-Gladrow, A lattice Boltzmann equation for diffusion, J. Stat. Phys. 79 (1995) 1023–1032.
[27] R.G.M. van der Sman, M.H. Ernst, Diffusion lattice Boltzmann scheme on a orthorhombic lattice, J. Stat. Phys. 94 (1999) 203–217.
[28] M. Hirabayashi, Y. Chen, H. Ohashi, The lattice BGK model for the Poisson equation, JSME Int. J. Ser. B 44 (2001) 45–52.
[29] M. Wang, J. Wang, S. Chen, Roughness and cavitations effects on electro-osmotic flows in rough microchannels using the lattice Poisson–Boltzmann methods, J. Comput. Phys. 226 (2007) 836–851.
[30] Z. Chai, B.C. Shi, A novel lattice Boltzmann model for the Poisson equation, Appl. Math. Model. 32 (2008) 2050–2058.
[31] P. Asinari, M.C. Quaglia, M.R. von Spakovsky, B.V. Kasula, Direct numerical calculation of the kinematic tortuosity of reactive mixture flow in the anode layer of solid oxide fuel cells by the lattice Boltzmann method, J. Power Sources 170 (2007) 359–375.
[32] Y. Suzue, N. Shikazono, N. Kasagi, Micro modeling of solid oxide fuel cell anode based on stochastic reconstruction, J. Power Sources 184 (2008) 52–59.

[33] C.-W. Wang, A.M. Sastry, Mesoscale modeling of a Li-ion polymer cell, J. Electrochem. Soc. 154 (2007) A1035–A1047.
[34] S. Link, W.-S. Chang, A. Yethiraj, P.F. Barbara, Anisotropic diffusion of elongated and aligned polymer chains in a nematic solvent, J. Phys. Chem. B 110 (2006) 19799–19803.
[35] P.M. Johnson, S. Faez, A. Lagendijk, Full characterization of anisotropic diffuse light, Opt. Express 16 (2008) 7435–7446.
[36] X. Zhang, A.G. Bengough, J.W. Crawford, I.M. Young, A lattice BGK model for advection and anisotropic dispersion equation, Adv. Water Resour. 25 (2002) 1–8.
[37] X. Zhang, A.G. Bengough, L.K. Deeks, J.W. Crawford, I.M. Young, A novel three-dimensional lattice Boltzmann model for solute transport in variably saturated porous media, Water Resour. Res. 38 (2002) 1167–1177.
[38] I. Ginzburg, Equilibrium-type and link-type lattice Boltzmann models for generic advection and anisotropic-dispersion equation, Adv. Water Resour. 28 (2005) 1171–1195.
[39] I. Rasin, S. Succi, W. Miller, A multi-relaxation lattice kinetic method for passive scalar diffusion, J. Comput. Phys. 206 (2005) 453–462.
[40] S. Suga, Stability and accuracy of lattice Boltzmann schemes for anisotropic advection–diffusion equations, Int. J. Mod. Phys. C 20 (2009) 633–650.
[41] P. Lallemand, L.-S. Luo, Theory of the lattice Boltzmann method: dispersion, dissipation, isotropy, Galilean invariance, and stability, Phys. Rev. E 61 (2000) 6546–6562.
[42] D. d'Humières, I. Ginzburg, M. Krafczyk, P. Lallemand, L.-S. Luo, Multiple-relaxation-time lattice Boltzmann models in three dimensions, Philos. Trans. R. Soc. London A 360 (2002) 437–451.
[43] X. He, N. Li, Lattice Boltzmann simulation of electrochemical systems, Comput. Phys. Commun. 129 (2000) 158–166.
[44] X. He, N. Li, B. Goldstein, Lattice Boltzmann simulation of diffusion–convection systems with surface chemical reaction, Mol. Simul. 25 (2000) 145–156.
[45] G. Drazer, J. Koplik, Tracer dispersion in two-dimensional rough fractures, Phys. Rev. E 63 (2001) 056104.
[46] X. Zhang, J.W. Crawford, A.G. Bengough, I.M. Young, On boundary conditions in the lattice Boltzmann model for advection and anisotropic dispersion equation, Adv. Water Resour. 25 (2002) 601–609.
[47] I. Ginzburg, Generic boundary conditions for lattice Boltzmann models and their application to advection and anisotropic dispersion equations, Adv. Water Resour. 28 (2005) 1196–1216.
[48] Y. Akinaga, S. Hyodo, T. Ikeshoji, Lattice Boltzmann simulations for proton transport in 2-D model channels of Nafion, Phys. Chem. Chem. Phys. 10 (2008) 5678–5688.
[49] M. Junk, A. Klar, L.-S. Luo, Asymptotic analysis of the lattice Boltzmann equation, J. Comput. Phys. 210 (2005) 676–704.
[50] M. Junk, Z. Yang, Asymptotic analysis of lattice Boltzmann boundary conditions, J. Stat. Phys. 121 (2005) 3–35.
[51] A. Caiazzo, M. Junk, M. Rheinländer, Comparison of analysis techniques for the lattice Boltzmann method, Comput. Math. Appl. 58 (2009) 883–897.
[52] S. Osher, R. Fedkiw, Level Set Methods and Dynamic Implicit Surfaces, Springer, New York, 2003.
[53] Y. Sone, Asymptotic theory of a steady flow of a rarefied gas past bodies for small Knudsen numbers, in: R. Gatignol, J.B. Soubbaramayer (Eds.), Advances in Kinetic Theory and Continuum Mechanics, Springer, Berlin, 1991, pp. 19–31.
[54] Y. Sone, K. Aoki, S. Takata, H. Sugimoto, A.V. Bobylev, Inappropriateness of the heat-conduction equation for description of a temperature field of a stationary gas in the continuum limit: examination by asymptotic analysis and numerical computation of the Boltzmann equation, Phys. Fluids 8 (1996) 628–638. erratum, ibid. 8 (1996) 841.
[55] Y. Sone, Kinetic Theory and Fluid Dynamics, Birkhäuser, Boston, 2002.
[56] T. Inamuro, M. Yoshino, F. Ogino, Accuracy of the lattice Boltzmann method for small Knudsen number with finite Reynolds number, Phys. Fluids 9 (1997) 3535–3542.
[57] G. Taylor, Dispersion of soluble matter in solvent flowing slowly through a tube, Proc. R. Soc. London A 219 (1953) 186–203.
[58] R. Aris, On the dispersion of a solute in a fluid flowing through a tube, Proc. R. Soc. London A 235 (1956) 67–77.
[59] M. Sussman, E. Fatemi, P. Smereka, S. Osher, An improved level set method for incompressible two-phase flows, Comput. Fluids 27 (1998) 663–680.
[60] F. Flin, J.-B. Brzoska, D. Coeurjolly, R.A. Pieritz, B. Lesaffre, C. Coléou, P. Lamboley, O. Teytaud, G.L. Vignoles, J.-F. Delesse, Adaptive estimation of normals and surface area for discrete 3-D objects: application to snow binary data from X-ray tomography, IEEE Trans. Image Process. 14 (2005) 585–596.
[61] F. Verhaeghe, S. Arnout, B. Blanpain, P. Wollants, Lattice-Boltzmann modeling of dissolution phenomena, Phys. Rev. E 73 (2006) 036316.
[62] S. Izquierdo, N. Fueyo, Momentum transfer correction for macroscopic-gradient boundary conditions in lattice Boltzmann methods, J. Comput. Phys. 229 (2010) 2497–2506.